RELATIONSHIPS BETWEEN EXTREME RAIN RATES AND CONVECTIVE INTENSITIES FROM THE PERSPECTIVES OF TROPICAL RAINFALL MEASURING MISSION AND WSR-88D RADARS

by

Alexandria C. Gingrey

A thesis submitted to the faculty of
The University of Utah
in partial fulfillment of the requirements for the degree of

Master of Science

Department of Atmospheric Sciences

The University of Utah

August 2017

The University of Utah Graduate School

STATEMENT OF THESIS APPROVAL

The thesis of **Alexandria C. Gingrey**

has been approved by the following supervisory committee members:

Edward J. Zipser	, Chair	**05/08/17** Date Approved
Adam Christopher Varble	, Member	**05/08/17** Date Approved
Gerald G. Mace	, Member	**05/08/17** Date Approved

and by **Kevin Perry** , Chair/Dean of

the Department/College/School of **Atmospheric Sciences**

and by David B. Kieda, Dean of The Graduate School.

ABSTRACT

Tropical Measuring Mission (TRMM) precipitation radar (PR) 2A25 V7 retrievals show that precipitation features (PFs) with the tallest maximum 40 dBZ echo heights are rarely the same PFs that exhibit the most extreme near-surface rainfall rates. To investigate the impacts of potential weaknesses in the 2A25 V7 retrievals, due to potential attenuation of the Ku-band signal, 14 years of June – August retrievals are compared to June – August 2014 hourly Weather Surveillance Radar – 1988 Doppler (WSR-88D) dual-polarimetric S-band data for 28 radars over the southeastern United States (SEUS). For more direct comparison, TRMM Ku-band measurements are converted to S-band approximations. Rain rates for WSR-88D data are approximated using the CSU-HIDRO algorithm, which calculates rain rates from reflectivity (Z), differential reflectivity (ZDR), and specific differential phase (KDP) relationships. This research aims to not only investigate the difference between TRMM PR and WSR-88D retrievals of reflectivity and rain rate, but also to investigate how apparent differences relate to TRMM path integrated attenuation (PIA), and WSR-88D KDP, ZDR and calculated hail fraction.

Tropics-wide TRMM retrievals confirm previous findings of a low overlap of extreme convective intensity and extreme near-surface rain rates. WSR-88D data also confirm that this overlap is low, but show that it is likely higher than TRMM PR retrievals indicate, approximately 30% higher in the SEUS for the 99th percentiles of maximum 40 dBZ heights and low-level rain rates. For maximum 40 dBZ echo heights that extend into

regions likely containing ice, mean WSR-88D reflectivities are approximately 2 dBZ higher than TRMM PR reflectivities. Higher WSR-88D-retrieved rain rates for a given low-level reflectivity combine with these higher low-level reflectivities to produce much greater mean WSR-88D rainfall rates than TRMM PR as a function of maximum 40 dBZ height, for heights that extend into regions likely to have ice. Investigations of TRMM PR PIA, and WSR-88D KDP, ZDR, and hail fraction indicate that the TRMM PR 2A25 V7 algorithm is possibly misidentifying low-mid level hail or graupel as greater attenuating liquid, or vice versa. This possible misidentification results in 2A25 V7 Z-R relationships that likely produce low biased rain rates in intense convection.

In dedication to my family for their unconditional encouragement and support.

TABLE OF CONTENTS

ACKNOWLEDGEMENTS

I would like to thank my advisors, Dr. Edward Zipser and Dr. Adam Varble, for their guidance and flexibility over the past three years. From opportunities working in the field, to countless hours spent in the William Browning Building, I am honored to have been able to work alongside scientists of such passion and esteem as you both, and hope to carry that passion and insight forth in my future endeavors. I would also like to thank Dr. Gerald Mace for serving on my committee. Special thanks are owed to Erich Carson, whose love, encouragement, and patience, even from a couple of states away, kept me strong and motivated. To my family and Erich's in Washington, as well as my friends and fellow Zipser group colleagues in Utah, I am immensely grateful for your continued positivity, support, and belief in me through the master's degree process.

I would like to thank the National Aeronautics and Space Administration for funding this research. I would also like to thank the National Oceanic and Atmospheric Administration and the National Climatic Data Center for providing the data used in this study. I would also like to acknowledge the Center for High Performance Computing at the University of Utah for providing the resources and troubleshooting necessary to complete this work.

CHAPTER 1

INTRODUCTION

The Tropical Rainfall Measuring Mission (TRMM), a joint effort between the National Aeronautics and Space Administration (NASA) and the Japanese Aerospace Exploration Agency (JAXA), provides scientists with tropics-wide precipitation retrievals from its launch in November 1997 through September 2014. The TRMM satellite was launched in an effort to provide not only a better understanding of tropical rainfall patterns, but also to understand their impacts on global hydrological and energy cycles (Simpson 1988; Kummerow 2000). Aboard TRMM were several instruments: the TRMM Microwave Imager (TMI), the Precipitation Radar (PR), the Visible Infrared Scanner (VIRS), the Lightning Imaging Sensor (LIS), and the Clouds and Earth's Radiant Energy System (CERES) (Kummerow et al. 1998). With a lifetime of 17 years, the database amassed via these instruments has provided invaluable information on rainfall characteristics across the tropics, including, but not limited to, diurnal patterns of convective systems (e.g., Nesbitt et al. 2003), tropical rainfall climatology (e.g., Alder et al. 2009; Wang et al. 2014), hurricane structures (e.g., Lonfat et al. 2004; Jiang et al. 2010, Hence et al. 2011), studies in regional variability of tropical convection (e.g., Peterson and Rutledge 2001), global distributions of convection (e.g., Liu and Zipser 2005; Zipser et al. 2006; Liu and Zipser 2007), patterns in stratiform rain, (e.g., Shumacher and Houze 2003),

and investigations of storm structure over land and ocean (e.g., Nesbitt et al. 2006).

To assess TRMM's accuracy, the TRMM Ground Validation (GV) effort was established at four sites throughout the tropics and subtropics: Melbourne, Florida; Houston, Texas; Kwajelin Atoll, The Republic of the Marshall Islands; and Darwin, Australia (Marks et al. 2000; Amitai et al. 2002; Wolff et al. 2005), providing both instantaneous and monthly precipitation products for comparison against TRMM observations. Using these sites, as well as rain gauge networks, various validation efforts have been carried out on TRMM rainfall estimates. Bolen et al. (2000) found that in cases of minimal attenuation, TRMM PR was within 1 dB of ground radar measurements, and in cases of higher attenuation, accurate estimates of Path Integrated Attenuation (PIA) could be retrieved. Through a comparison study between TRMM PR retrievals and retrievals from the Melbourne, FL WSR-88D radar, Liao et al. (2001) also found that TRMM PR was within 1 dB of the WSR-88D retrievals throughout the mean vertical reflectivity profile. They also discovered that TRMM PR and WSR-88D retrievals were better correlated in stratiform than convective precipitation. Islam et al. (2012) found that the best precipitation estimates came from a combination of the PR and TMI data, however, the PR rain rates alone needed improvement, especially in convective precipitation. Kirstetter et al. (2013) found that Version 7 (V7) of the 2A25 rainfall algorithm was superior to previous versions and had improved rain rate estimates over land.

Despite overall good agreements shown in comparisons between TRMM retrievals and ground observations, TRMM PR's 2A25 rain rate algorithm (Iguchi et al. 2000) is imperfect and potentially biased for some situations, especially for precipitation with severe convective intensity (Iguchi et al. 2009; Kozu et al. 2009). Comparing TRMM PR

2A25 Version 6 data to WSR-88D from Melbourne, FL, Liao and Meneghini (2009) found that, at the surface, TRMM PR attenuation estimates are underestimated in convection; and in especially heavy precipitation, TRMM PR calculated rain rates were 19% less than those of WSR-88D. Iguchi et al. (2009) express that revisions to the PR 2A25 algorithm have been necessary due to issues with nonphysical retrievals and inconsistency between PR and TMI estimates. Such revisions have improved retrieval accuracy over the ocean, but still result in an underestimation of rainfall rates calculated over land (Iguchi et al. 2009). One source for this error arises from attenuation correction. The TRMM PR is a Ku-band radar, operating at a frequency of 13.8 GHz, and is therefore susceptible to significant attenuation from liquid and partially melted hydrometeors.

As outlined by Iguchi et al. (2000, 2009), there are three steps to retrieve a rain rate value in the 2A25 algorithm. The first converts the retrieved PR power measurement P_r to the apparent reflectivity factor Z_m, which is then converted to the effective radar reflectivity factor Z_e. Z_e is then converted to rainfall rate R for the third step. Within conversion from Z_m to Z_e lies adjustments for nonuniform beam filling (NUBF) effects and signal attenuation sources: precipitation k_p, cloud liquid water k_{clw}, water vapor k_{wv}, and molecular oxygen k_{O2}. The PIA for a data column is twice the sum of the contributions from each of these attenuation sources throughout the column, with the largest source of attenuation being k_p. While the specific equations utilized in the 2A25 algorithm are described in Iguchi et al. (2009), a brief summary of the attenuation correction is as follows. The 2A25 algorithm utilizes the Hitschfeld-Bordan (H-B) method (Hitschfeld and Bordan 1954) and surface reference technique (SRT) (Iguchi and Meneghini 1994; Meneghini et al. 2000) to calculate the PIA for a given column. The H-B method uses the well-established power

law relationship, $k = \alpha Z_e^{\beta}$ (k is the specific attenuation coefficient, Z_e is the true reflectivity factor, and α and β are parameters dependent on particle size distributions and phase) to produce an estimate of PIA at the farthest range of the rain echo, however, it is only effective in cases of low attenuation (Hitschfeld and Bordan 1954; Iguchi and Meneghini 1994). The SRT method, which is effective in managing larger attenuation, uses the offset between a rain-free surface cross-section and the measured surface cross-section when precipitation is present to produce a PIA estimate at the near-surface rain echo. Both the H-B method and the SRT method show their strengths where the other has weaknesses, and therefore a hybrid of these two methods is used in producing a PIA correction in the data column (Iguchi and Meneghini 1994; Iguchi et al. 2000, 2009).

Attenuation calculations are completed in two cycles. The first cycle produces an attenuation corrected reflectivity profile and a rainfall rate estimate near the surface using a Z-R relationship (Iguchi 2000, 2009). Using the GPROF numerical model from Kummerow et al. (2001), this surface rainfall rate is associated with a vertical profile of cloud liquid water that then provides an estimated k_{clw} in each vertical bin. Estimated surface temperature and relative humidity allow for an approximation of k_{wv} at each vertical level, and k_{O2} is estimated as a function of altitude. These attenuation estimates are then used to apply an attenuation correction to the original Z_m profile, which can then be corrected for solely precipitation to obtain the final Z_e vertical profile and corresponding rainfall rate estimates (Iguchi et al. 2009). This final rainfall rate estimate is determined from a Z-R relationship,

$$R = a\, Z_e^b \tag{1.1}$$

where a and b are coefficients determined by the rain type and height of the melting level,

as determined by the 2A23 algorithms (Iguchi et al. 2009). These parameters are then modified based on an assumed drop size distribution (DSD) modeled from Kozu et al. (2009), which varies for stratiform and convective rain.

In convective rain especially, problems can arise if the 0° C height is misrepresented. In V7 of the 2A25 algorithm, a separate set of $k_p - Z_e\ (\alpha, \beta)$ and $Z_e - R\ (a, b)$ parameters are given for use in the assumed ice region (above the -15° C height), at 750 m above the 0° C height, at the 0° C height, and at 750 m below the 0° C height, respectively, with a linear interpolation of the parameters in altitudes between these levels (Iguchi et al. 2009). With an incorrect assumption of the melting level height comes the misidentification of true particle phase. This is especially a problem when the assumed melting level is higher than the true melting level, resulting in ice particles being identified as liquid, which attenuate significantly more than ice does. This leads to improper $k_p - Z_e$ *and* $Z_e - R$ parameters used, and because ice particles attenuate less than liquid, a higher attenuation is estimated than what is actually in existence within the column. As previously stated, high attenuations are estimated and resolved via the SRT method, which produces a negative rain bias in these conditions (Iguchi et al. 2009) due to a combination of both the PIA offset as well as the previously mentioned changes of the *a* and *b* parameters in the $Z_e - R$ calculation. This issue is common when the storm tops are high (Kozu et al. 2009; Iguchi et al. 2009).

Zipser et al. (2006) utilized the TRMM database to show where the most convectively intense precipitation features exist throughout the tropics and subtropics (from 36 °N to 36 °S). One of the proxies used in their study was the maximum height of the 40 dBZ echo, where taller 40 dBZ echoes are indicative of more convectively intense

systems (Zipser and Lutz 1994). It thus follows, that these convectively intense, tall systems are prone to underestimated rainfall rates as per the aforementioned attenuation correction biases when mixed-phase or rain attenuation parameters are used in ice particle regions or vice versa (Iguchi 2009). Rasmussen et al. (2013) expanded upon this to show that rain rate underestimation was present among differing types of extreme precipitation, and was especially problematic for systems exhibiting mixed phase and frozen hydrometeors. Thus there is no question that the TRMM PR algorithm is imperfect, especially in extreme convection and precipitation, but the extent to which it may be biased as a function of convective intensity is still unclear.

This uncertainty impacts findings such as those established in Hamada et al. (2015), a study which investigates the correlation between systems with extreme near-surface rain rate and those with extreme maximum 40 dBZ echo height. By analyzing the overlap of TRMM PR observed precipitation features (PFs) containing a maximum 2A25 pixel rainfall rate in the top 0.1% (99.9^{th} percentile) of all PF maximum pixel rainfall rates and those with a maximum 40 dBZ echo height in the top 0.1% (99.9^{th} percentile) of all PF maximum 40 dBZ heights, Hamada et al. (2015) discovered that little overlap exists between the "tallest" and "rainiest" thunderstorms. Because their study focuses on only the top 0.1% (99.9^{th} percentile) most extreme PFs, it is possible that attenuation correction issues could bias the magnitude of this overlap. If rainfall rates are being significantly underestimated due to attenuation correction biases, then the reported dichotomy between the tallest and rainiest storms may be exaggerated beyond what is true. This potential issue serves as the primary motivation for this study. Investigating extreme convective intensity, extreme precipitation rates, and to what extent they overlap, serves as further motivation.

These extremes are often associated with severe weather systems, such as supercells and flooding events, which can have devastating societal impact. It is thus important to explore how satellites such as TRMM observe these extremes and to work towards more accurately depicting extreme events, especially considering many regions have inadequate ground radar networks, or none at all, and therefore rely on satellite observations.

To investigate the accuracy of TRMM PR reflectivities and rainfall rates, they can be compared to radar observations from Weather Surveillance Radar – 1988 Dopplers (hereafter WSR-88Ds), which are S-band radars operating at 2.7-3 GHz, and are thus minimally impacted by attenuation in precipitation. The WSR-88Ds also have dual-polarization capability which provides additional information on hydrometeor characteristics that are not retrievable by TRMM. The National Oceanic and Atmospheric Administration (NOAA) WSR-88D network was deployed throughout the United States in the 1990s under the Next Generation Weather Radar (NEXRAD) program (Crum et al. 1993). Through 2011, WSR-88Ds provided near real time reflectivity, radial velocity, and spectral width data, as well as many associated and derived products that were used by both the operational weather forecasting and research communities. By the end of 2013, WSR-88Ds had been upgraded from single polarization to dual-polarization radar systems, allowing for the transmittal and reception of both horizontally and vertically oriented radar waves (Cunha et al. 2015). This upgrade allowed for measurement of dual-polarization variables that provide additional information on particle number and shape, two of which are important to rain rate retrievals used in this study: specific differential phase (KDP) and differential reflectivity (ZDR).

As described by Chandrasekar et. al (2008) and Istok et al. (2009), KDP expresses

the change in the differential phase between the horizontal and vertical waves as a function of range. Propagation of a radar wave slows down as it moves through hydrometeors, and the horizontal and vertical pulses slow at different rates if particle dimensions differ between the horizontal and vertical dimensions. Medium to large-sized raindrops are oblate with greater widths than heights, causing the horizontal pulse to slow more than the vertical pulse, which then creates a phase shift between them. This phase shift is not only sensitive to the hydrometeor asphericity, but also to the number concentration of aspherical hydrometeors without sensitivity to signal attenuation because it is not a power measurement. Additionally, it responds little to hail because tumbling hail in a volume is close to spherical. Therefore, KDP provides critical information on the rainwater content in conditions with hail contamination or signal attenuation that are common in intense convection. ZDR, on the other hand, expresses the difference in the horizontal (Z_h) and vertical (Z_v) pulse power returns to the radar, where:

$$ZDR = 10 \log\left(\frac{Z_h}{Z_v}\right) \tag{1.2}$$

A positive ZDR value indicates that the presence of hydrometeors that are wider than they are tall, and a negative ZDR indicates the opposite. ZDR helps in rain rate retrievals in that conditions with significant numbers of oblate raindrops produce greater horizontal reflectivity returns than vertical reflectivity returns, producing an overestimate of rain rate if horizontal reflectivity is used alone, as in traditional Z-R relationships such as those used for the TRMM PR 2A25 algorithm.

Ryzhkov and Zrnić (1996) show that rain rates calculated via a KDP-R relationship agree well with surface rain gauges as KDP does not respond to hail or suffer from attenuation like reflectivity. Gorgucci et al. (1993) show that Z-ZDR-R and ZDR-R

relationships are effective in estimating rain rates across a range of ZDR values. A diverse array of options in calculating rainfall estimates is possible with these variables, with multiple equations employed in the WSR-88D Quantitative Precipitation Estimate (QPE) method. This method uses several parameters, including hydrometeor identification (HID) and the height of the melting level, to determine which rain rate relationship, using Z, ZDR, and KDP, is appropriate (Berkowitz et al. 2013; Cunha et al. 2015). The precise QPE algorithm being employed, however, is difficult to ascertain for a given WSR-88D radar and time. Therefore, in this study, the CSU-HIDRO algorithm (Cifelli et al. 2011) is utilized, which allows for choices to the coefficients in the Z-R, Z-ZDR-R, Z-ZDR-KDP, and Z-KDP relationships, as well as the particle identification (PID) utilized, as discussed more in Chapter 2. The CSU-HIDRO algorithm, shown by Cifelli et al. (2011) to have minimal bias in heavy rain and hail events, uses a logic chart, depicted here in Figure 2.1, to decide which rain rate relationship to use in different situations.

The work in this thesis aims to investigate relationships between maximum 40 dBZ echo heights, near surface rain rates, and near surface reflectivities, to evaluate the robustness of the overlap magnitude between extreme convective intensity and extreme rain rates found in Hamada et al. (2015). This is done by analyzing overlap relationships in both TRMM PR and WSR-88D retrievals over the southeastern United States. Differences in TRMM and WSR-88D perspectives are used to identify potential TRMM PR retrieval biases with investigation of WSR-88D KDP, ZDR, and PID, and TRMM PR 2A25 PIA estimates in an attempt to partially explain potential biases. Data and methods used are described in Chapter 2, with results of TRMM PR observations between 36° N and 36° S and a focused comparison of TRMM PR observations compared against WSR-

88D observations in the southeastern United States in Chapter 3. Chapter 4 investigates WSR-88D KDP, ZDR, and hail fraction, and TRMM PR 2A25 PIA estimates, and conclusions are provided in Chapter 5.

CHAPTER 2

DATA AND METHODS

2.1 TRMM Data

The TRMM PR's seventeen years in orbit amassed a robust collection of observations across the tropics and subtropics from 36 °N to 36 °S. As the TRMM PR scanned, retrievals were saved in the form of columns with 80 vertical levels, with 250-m intervals between each level. The horizontal spacing of these columns is ~4.5-km post-orbit boost, which occurred in August 2001. These data are housed in a number of collections, and for this study, were accessed from the University of Utah PF Database (Liu et al. 2008). The PF Database contains both Level-One Version-7 (hereafter V7) data columns, as well as Level-Two data where PFs consisting of 4 or more contiguous columns with near-surface reflectivity of 20 dBZ or greater have been defined and saved with their characteristics separately. Reflectivities and rain rates associated with individual columns are primarily used in this research, although entire PFs characteristics are also used for the domain between 36 °N and 36 °S for appropriate comparison with Hamada et al. (2015).

2.2 WSR-88D Data

The current National Oceanic and Atmospheric Administration (NOAA) WSR-88D network consists of 160 radars across the United States, U.S. territories, and South

Korea. The network over the southeastern United States (hereafter SEUS) does not suffer from coverage gaps to the extent that the southwestern United States does, and also exhibits more frequent and convectively intense systems than the southwestern United States. Therefore, 28 radars (Table 2.1) from the southeastern United States are chosen for comparison with TRMM PR observations. WSR-88D data were downloaded via the online archived inventory provided by the National Climatic and Data Center (NCDC) for June through August 2013. Unless down for maintenance or temporary failure, WSR-88D radars constantly operate, saving data in radial scan format. For this comparison, only scans that occur within five minutes of each hour were saved to avoid too much correlation between scans and to limit the size of a large dataset, all while avoiding diurnal biases. WSR-88D radars operate multiple scanning strategies dependent on the current conditions at the radar. Because potential TRMM PR errors in deep convective systems are of primary concern, only WSR-88D data from convective volume coverage patterns 11, 211, 12, and 212 are saved, which contain more upper tilt elevation angles than other patterns.

2.3 Methodology for Comparison

Comparisons of V7 TRMM PR retrieved data columns with WSR-88D observed columns are a primary focus. WSR-88Ds are constantly operating over their domain, aside from when they are shut down for maintenance or experience temporary failure. TRMM PR, however, captures limited snapshots of systems as it orbits overhead. Therefore, for a robust assessment, individual columns of reflectivity are used to investigate how vertical reflectivity profiles, calculated rain rates, and maximum heights of the 40 dBZ reflectivity echo vary between TRMM PR and WSR-88D, by comparing numerous vertical data

columns observed by TRMM PR during the months of June, July, and August (JJA) from 2002 through 2014 with numerous vertical data columns observed by WSR-88D during JJA 2013 over the southeastern United States.

2.3.1 TRMM Data Processing

A database of TRMM PR 2A25 data columns is created by filtering V7 data for the ensuing conditions. JJA months are selected since systems during these months are predominantly convective over the southeastern United States, and post-boost years (2002-2014) are used to maintain consistent horizontal resolution for comparison to WSR-88D data. Second, columns must have a reflectivity of 20 dBZ or greater at 1.5-km altitude, indicating likely precipitation at the surface. 2A25 saves several "near-surface" variables, however, this altitude is not constant for every column because the TRMM PR swath extends closest to the surface at nadir, and is truncated at about 1.0 – 1.5 km above the surface at the swath edges to avoid contamination from surface clutter. Therefore, for uniformity, 1.5-km altitude is used to maximize data retention, avoid ground clutter issues, and maintain full vertical profiles for the WSR-88D radars out to 80 km away from the radar. Columns must occur within 80 km of one of the WSR-88D radars listed in Table 2.1 to avoid geographical biases since TRMM observes uniformly at a given latitude, while WSR-88D radars are nonuniformly spaced. Additionally, the southeastern United States straddles the northern edge of TRMM's orbit where the TRMM PR sampled significantly more frequently at about 34 °N than near 30 °N. The 80-km limit is in place as it is the distance from the WSR-88D at which WSR-88D data can no longer be retrieved at 1.5-km altitude and vertical resolution degrades to the point of being questionable for comparison

to retrieved TRMM PR profiles. For each column that meets these criteria, the following variables are saved: reflectivity (dBZ) at all 80 vertical levels, TRMM PR retrieved rain rate at 1.5-km altitude, path-integrated attenuation (PIA), time, date, latitude, longitude, and the WSR-88D radar to which it corresponds.

The TRMM PR operates at Ku-band at a frequency of 13.8 GHz, while the WSR-88D operates at S-band at a frequency of 2.7 – 3 GHz. Hydrometeors create different scattering effects at different radar frequencies. Therefore, to conduct fair comparisons of reflectivity retrievals between TRMM PR and WSR-88D, a second dataset of TRMM PR reflectivity converted to estimated S-band equivalent values is saved. This conversion is conducted following Cao et al. (2013) by first calculating an S-Ku reflectivity difference, and then adding this value to the initial TRMM Ku-band retrievals. Separate conversions are applied to distinctive regions within the vertical reflectivity profile, as Ku-band retrieves higher reflectivities than S-band in the rain region and lower reflectivities in the ice region when large particles are present, due to Mie scattering effects. The conversion algorithms in each region are determined via simulations using assumed scattering and microphysical models for corresponding hydrometeor phase. In the rain region, assumed here to be between 0 – 3.5-km altitude, the following conversion is applied where R is TRMM PR Ku-band reflectivities in dBZ:

$$\mathrm{DFR(S\text{-}Ku)} = 0.0478 + (0.0123\,R) + (-3.504 \times 10^{-4}\,R^2) + (-3.3 \times 10^{-5}\,R^3) + (4.27 \times 10^{-7}\,R^4) \quad (2.1)$$

In the ice region, assumed to exist above 5-km altitude, the following conversion, which is more appropriate for hail than snow, is applied:

$$\mathrm{DFR(S\text{-}Ku)} = 0.088 + (5.39 \times 10^{-3}\, R) + (-2.99 \times 10^{-4}\, R^2) + (1.9 \times 10^{-5}\, R^3) \quad (2.2)$$

Conversions are not performed between 3.5 and 5-km altitudes where the melting level typically resides in the SEUS summer. It should be noted that these relationships have the potential to be biased should the actual hydrometeor properties be different than what is assumed in the generation of these conversions. Overall, the conversion creates a database of S-band equivalent (TRMM-S) TRMM PR reflectivities for more appropriate comparison to WSR-88D S-band reflectivities.

2.3.2 WSR-88D Data Processing

WSR-88D radial scans have a resolution of 0.5-km by 1-degree which, for comparison to TRMM PR grids, needs to be interpolated to a Cartesian grid. Gridding is completed using Radx software, developed by the National Center for Atmospheric Research (https://github.com/NCAR/lrose-core, https://www.eol.ucar.edu/content/lidar-radar-open-software-environment). Radial scans are first interpolated to a horizontal grid spacing of 1.125 km and vertical grid spacing of 250 m, but are then horizontally averaged to match TRMM PR's horizontal resolution of 4.5 km.

The initial gridding from the Radx2grid routine produces a 160 x 160 x 80 grid of reflectivity, correlation coefficient (RHO), latitude, and longitude. The same scans are additionally processed with the RadxPartRain routine to produce a corresponding 160 x 160 grid of rain rate, specific differential phase (KDP), differential reflectivity (ZDR), particle identification (PID), latitude, and longitude at an altitude of 1.5 km. Rain rate calculations are completed using the CSU-HIDRO algorithm defined in Cifelli et al. (2011). While the TRMM PR applies a reflectivity-rain rate (Z-R) relationship drawing

from a prescribed drop-size distribution model (Kozu 2009), the CSU-HIDRO algorithm uses reflectivity, PID, KDP, and ZDR to select from the following rain rate relationships (Rhyzkov and Zrnic 1995; Brandes et al. 2001, 2002) as defined in the CSU-ICE algorithm in Cifelli et al. (2011):

$$\mathrm{R(Z)} = 0.017(Z)^{0.7143} \tag{2.3}$$

$$\mathrm{R(KDP)} = 40.5(KDP)^{0.85} \tag{2.4}$$

$$\mathrm{R(KDP, ZDR)} = 90.8(KDP)^{0.93} \text{ x } 10^{-0.169(ZDR)} \tag{2.5}$$

$$\mathrm{R(Z, ZDR)} = 6.7\text{E-}3(Z)^{0.927} \text{ x } 10^{-0.343(ZDR)} \tag{2.6}$$

to calculate the rain rate at a given grid point, as illustrated in Figure 2.1. As seen in Figure 2.1, the CSU-HIDRO algorithm does not retrieve a rain rate when the PID indicates hail or graupel. In rain-hail or rain-graupel mixtures, only rain rate is calculated using Equation 2.4 if KDP is greater than or equal to 0.3. In liquid, pixels with KDP values greater than or equal to 0.3 and reflectivities greater than or equal to 38 dBZ utilize Equation 2.5 to calculate rain rate when corresponding ZDR values are greater than or equal to 0.5, and use Equation 2.4 where ZDR is less than 0.5. Also in liquid, pixels with KDP less than 0.3 or corresponding reflectivities less than 38 dBZ, employ Equation 2.6 when corresponding ZDR values are greater than or equal to 0.5, and use Equation 2.3 when ZDR is less than 0.5.

Before these high-resolution gridded variables are averaged down to match the 4.5-km horizontal grid spacing of TRMM PR, the data are quality controlled based on the following criteria. First, the grid points at 1.5-km altitude are filtered to remove non-meteorological returns. Nonmeteorological returns are determined using both the PID and the correlation coefficient. One of 16 PIDs are chosen for each grid point via a series of

conditional thresholds and ranges for a number of radar retrieved variables, including, but not limited to, ZDR, KDP, and RHO. There are three nonmeteorological classifications for PIDs: flying insects, second trip echoes, and ground clutter. Grid points with these classifications, as well as their corresponding column in the 160 x 160 x 80 grid, are set to null values. The correlation coefficient is also used to discern valid returns, as values less than 0.7 are indicative of insects, ground clutter, or significant attenuation, and therefore, these points as well as their corresponding columns are set to null values. This limits the possibility that reflectivity and retrieved rain rate at 1.5-km altitude are biased because of invalid values.

To degrade the high-resolution 1.125-km grids to 4.5-km, variables in each 4 x 4 set of grid points are averaged to produce a value for the new grid point on the 4.5-km grid. Grid points that do not contain valid echoes are set as null values. Before degrading from 1.125 to 4.5-km resolution, reflectivity is converted from dBZ to reflectivity factor, Z_e, using Equation 2.7:

$$Z_e = 10^{\frac{dBZ}{10}} \tag{2.7}$$

Once the values of Z_e are averaged, they are converted back to units of dBZ using Equation 2.8:

$$dBZ = \log(Z_e) * 10 \tag{2.8}$$

During degradation, the hail fraction in each new grid box, defined as the area within each grid box impacted by ice, is added to the dataset for each radar. There exist four PID categories that are indicative of hail or graupel presence: hail, rain-hail mixture, graupel-small hail, and graupel-rain. Hail fraction is calculated by tallying the frequency of these four identifications within each 4 x 4 set of grid points, and dividing it by 16 (the number

of grid points being averaged). With the knowledge of the hail fraction, it can be determined how much the other variables at a given grid point may be affected by ice contamination at 1.5-km altitude.

Every WSR-88D exhibits a "cone of silence" centered over the radar where the radar does not observe the entire troposphere with the altitudes not observed being dependent on range. Vertically incomplete scans are also present at greater distances from the radar, as the lowest 0.5-degree elevation angle beam height increases with distance from the radar because of atmospheric refraction and the Earth's curvature. In order to assure that WSR-88D columns contain data between 1.5 and 15-km altitudes, columns are only saved for comparison if they exist within an annulus ranging from 40 km – 80 km from the radar location. As with TRMM, columns are retained only if they exhibit a reflectivity of 20 dBZ or greater at 1.5-km altitude.

Once all columns have been saved for both the TRMM PR and WSR-88D datasets, there exists a differing number of total columns in each dataset for each radar. To avoid potential biases due to the differing sample sizes of the datasets, the saved columns in the larger of the two datasets are randomly sampled down to the size of the smaller dataset for each radar. For example, the number of TRMM PR and WSR-88D observed columns at radar KBMX is 28,301 and 34,504, respectively. The TRMM PR columns have the limiting sample size in this case, and therefore the WSR-88D dataset is randomly sampled down to 28,301 columns for comparison. Once this subsampling at each of the 28 radars is completed, there exists a set of TRMM PR observed columns, TRMM-S calculated columns, and WSR-88D retrieved columns that are ready for comparison, which are referred to as the TRMM-Ku, TRMM-S, and WSR-88D datasets, respectively.

Table 2.1 Locations (City, State) of the 28 WSR-88D radars used in this study.

List of utilized WSR-88Ds			
Radar	Location	Radar	Location
KBMX	Birmingham, AB	KJAX	Jacksonville, FL
KCAE	Columbia, SC	KJGX	Robins AFB, GA
KCLX	Charleston, SC	KLCH	Lake Charles, LA
KDGX	Jackson, MS	KLIX	New Orleans, LA
KDYX	Dyess AFB, TX	KLZK	Little Rock, AR
KEOX	Ft. Rucker, AB	KMOB	Mobile, AB
KEVX	Eglin AFB, FL	KMXX	Montgomery – Maxwell AFB, AB
KFDR	Frederick, TX	KNQA	Memphis, TN
KFFC	Atlanta, GA	KPOE	Ft. Polk, LA
KFWS	Dallas – Ft. Worth, TX	KSHV	Shreveport, LA
KGRK	Ft. Hood, TX	KSRX	Ft. Smith, OK
KGSP	Greenville – Spartanburg, SC	KTLH	Tallahassee, FL
KGWX	Columbus AFB, MS	KTLX	Oklahoma City, OK
KHTX	Huntsville – Hytop, AB	KVAX	Moody AFB, GA

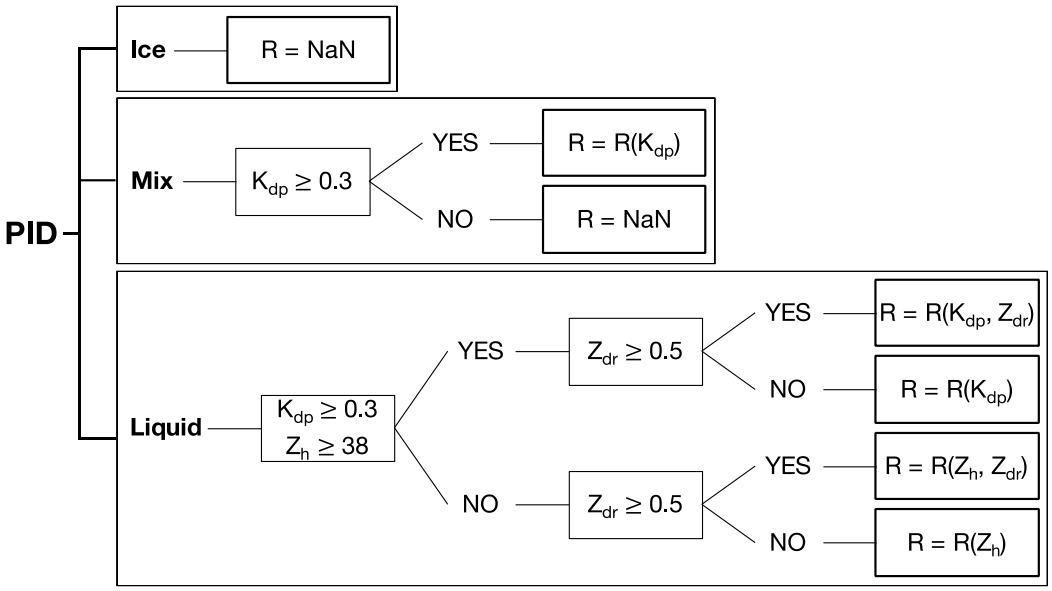

Figure 2.1 Flowchart depicting the CSU-HIDRO algorithm logic. Adapted from Figure 3 in Cifelli et al. 2011.

CHAPTER 3

RAIN RATE, REFLECTIVITY, AND MAXIMUM 40 DBZ HEIGHT RELATIONSHIPS

3.1 TRMM PR Retrievals Across the Tropics and Subtropics

3.1.1 TRMM PR Observed Precipitation Features

Using the maximum height of the 40 dBZ echo as a proxy for convective intensity (e.g., Zipser et al. 2006), the overlap fraction between the most convectively intense TRMM PR precipitation features (PFs) and those with the highest near-surface pixel rainfall rates is shown as a function of location in Figure 3.1. The use of the 99.5th percentile narrows systems to those that are especially extreme, without overly restricting the number of systems being examined. This overlap perspective follows a methodology similar to that used in Hamada et al. (2015), and supports their finding that the PFs with the tallest 40 dBZ echo heights are rarely the features with the highest near-surface rainfall rates, with overlap fractions mainly ranging from 0 to 0.3 over land. The overlap fractions over the ocean are higher, generally ranging from 0.2 to 0.5 over regions with significant rainfall. The highest overlap fractions, up to approximately 0.7, exist in relatively dry subtropical regions of atmospheric subsidence, which are regions of stratocumulus and trade cumulus, with deep convection not only being relatively rare, but also possessing a narrower range of convective intensity than most other regions, especially over land. This overlap contrast

between land and ocean may be related to the existence of more intense convection over land than over ocean (Zipser et al. 2006). However, part of this contrast may result from significant TRMM PR attenuation and imperfect assumptions regarding attenuation correction and Z-R relationships used in intense continental deep convection, which serves as motivation for validation of the overlap conclusions in Hamada et al. (2015).

Despite lower overlap fractions, there are many regions over land that express non-negligible numbers of systems that are both in the 99.5th percentile of convective intensity and rainfall rates for that given region. The southeastern United States (hereafter SEUS) from 25° N - 35° N and 80° W - 100° W, exhibits fractions from 0.05 – 0.3, making it a region that appears representative of overlap fractions in other land regions across the tropics and subtropics. This, coupled with the extensive geographical coverage of the WSR-88D dual-polarimetric S-band radar network, provides an opportunity for validating TRMM PR observations of convectively intense and extreme rain rate systems over the SEUS domain with possible implications for interpretation of TRMM PR rainfall estimates across the entire tropics and subtropics.

3.1.2 TRMM PR Observed Columns

The same calculation of overlap fraction is shown in Figures 3.2(a)-(c), however, rather than examining the overlap fraction of PF characteristics, we examine the overlap fractions of characteristics within individual TRMM PR observed vertical data columns in each 5° x 5° box. Later comparisons between TRMM PR and WSR-88D require the use of vertical columns rather than PFs due to the differing observation geometries of the two radars. WSR-88D scans from the ground, and due to increasing beam height and width at

far ranges, as well as the "cone of silence" at the radar center, PFs cannot be defined in the same manner as done for TRMM PR data. Thus, data columns are more directly comparable between the two datasets.

In Figures 3.2(a)-(c), an overlap fraction of 1 indicates that the 99.5th percentile values of both variables are always observed in the same data columns in a given grid box. The overlap fractions of maximum 40 dBZ heights and near-surface rainfall rates (3.2a), as well as maximum 40 dBZ heights and near-surface reflectivities (3.2b) are very small over the entire domain, indicating that it is very uncommon for the same vertical column observed by TRMM PR (~20 km^2 in horizontal area) to exhibit extremes in both convective intensity and rainfall rate, or extremes in both convective intensity and near-surface reflectivity, over both land and ocean.

The small overlap fractions, no greater than 0.4, between maximum 40 dBZ height and near-surface rainfall rate in Figure 3.2(a) further support the Hamada et al. (2015) conclusion that convective intensity proxies do not always correlate with extreme rainfall rates at the surface. Overlap fractions in maximum 40 dBZ echo heights and near-surface rain rates seen in the column perspective (Figure 3.2) are much lower, especially over the oceans, than were shown from the PF perspective (Figure 3.1). This is likely because the PFs in Figure 3.1 are a collection of columns, therefore, it is much more likely that a feature will contain columns that are in the top percentiles of the two variables being compared than it is for a single column to fall in the top percentiles for both variables being compared. A similar result is found in Figure 3.2(b), comparing maximum 40 dBZ heights and near-surface reflectivity, which is expected because near-surface reflectivity is used to calculate near-surface rain rate with Z-R relationships (Iguchi et al. 2009). Overlap fractions here

are slightly higher across the domain than in Figure 3.2(a), but still do not exceed 0.4.

When comparing near-surface rain rates and near-surface reflectivities (Figure 3.2(c)), the majority of the TRMM domain exhibits higher than a 0.5 overlap fraction between extreme near-surface rainfall rates and near-surface reflectivities, which again is expected due to the use of near-surface reflectivity in the calculation of near-surface rain rate via a Z-R relationship (Iguchi et al. 2009). In each comparison (Figure 3.2(a)-(c)), the SEUS domain exhibits overlap fractions comparable to most other land areas, and thus, even from the column perspective, it remains a good location with a robust dataset for validating TRMM PR vertical column observations.

Figure 3.3(a)-(c) shows the overlap fractions of maximum 40 dBZ echo heights and near-surface rainfall rates at 90^{th}, 95^{th}, and 99^{th} percentiles throughout the tropics and subtropics. Across all top percentiles (Figure 3.3(a)-(c)), a similar result is produced, where there is generally a low overlap fraction (not exceeding 0.5 over land) between extreme maximum 40 dBZ echo heights and extreme near-surface rain rates. As the percentiles change from the 99^{th} (Figure 3.3(a)) to the 90^{th} (Figure 3.3(c)), the overlap fractions increase, ranging between 0.05 and 0.15 over the SEUS for the 99^{th} percentile, to between 0.35 and 0.4 for the 90^{th} percentile. This overlap fraction increase can be attributed to an increase in the fraction of the column sample size within the top percentiles as the percentiles lessen. In agreement with the 99.5^{th} percentile (Figure 3.2), there is little contrast between land and ocean from the column perspective, and for the 90^{th} percentile, the overlap fraction may even be greater over land than ocean, but the reason for this is unknown. At the 90^{th}, 95^{th}, and 99^{th} percentiles, (Figure 3.3(a)-(c)), the SEUS domain exhibits overlap fractions comparable to most other land and ocean areas, and thus, remains

a good location for validating TRMM PR retrievals.

3.1.3 TRMM PR PF Reflectivity, Rain Rate, and Maximum 40 dBZ Height Comparisons

A preliminary look at how maximum 40 dBZ echo height, near-surface rain rate, and near-surface reflectivity relate to one another in PFs across the TRMM domain is shown using a variable filled joint histogram in Figure 3.4. The overlap fraction for the top percentiles (90^{th}, 95^{th}, 99^{th}, and 99.5^{th}) is shown to decrease as the percentiles become more extreme, which is a result of the sample sizes within the overlap region decreasing as the top percentile is increased. The resulting low overlap between extreme maximum 40 dBZ heights and extreme near-surface rain rates shown in Figures 3.2(a) and Figure 3.3(a)-(b) is also seen here, most evidenced by the 99.5^{th} and 99^{th} percentile lines, where the most extreme maximum 40 dBZ echo heights coincide with near-surface rain rates of ~50 mm hr^{-1}, which is lower than the thresholds, 63 and 80 mm hr^{-1}, respectively, for these top percentiles. Figure 3.4 also shows that PFs with the highest near-surface rain rates (50-300 mm hr^{-1}) have the highest probability of a maximum 40 dBZ height of ~5 km. Considering that this is near or just above the melting level, this area of the distribution could be significantly impacted by attenuation error via the misidentification of particles as ice when they are liquid, or vice versa (Iguchi 2009). Additionally, columns with extreme maximum 40 dBZ heights are subject to attenuation correction biases, providing further motivation for comparisons of TRMM PR results against the WSR-88D dataset.

Variable filled probability density functions are shown in Figure 3.5 for PFs occurring over land (3.5a), ocean (3.5b), and the SEUS (3.5c), rather than all of the tropics and subtropics combined (Figure 3.4). In agreement with Figure 3.4, PFs over

land with the highest maximum near surface rain rates (over 150 mm hr^{-1}) have the highest probability of exhibiting a maximum 40 dBZ height between 4 and 6 km. Also in agreement with Figure 3.4, PFs over land with the highest maximum 40 dBZ heights, up to 15 km, have the highest probability of being associated with more moderate rain rates. Over the oceans (3.5b), PFs are not as convectively intense as over land, with maximum 40 dBZ heights rarely exceeding 8 – 9 km, and they also exhibit less extreme rain rates than seen over land. Figure 3.5c shows results over the SEUS, as it is used as the region for evaluation of TRMM PR using WSR-88D in this study. The SEUS is justified as a viable region for validating TRMM PR retrievals as it is shown to be comparable to other tropical and subtropical land regions. Similar to 3.5a, the SEUS exhibits tall (up to 16 km) maximum 40 dBZ echo heights that are tallest when associated with relatively moderate rain rates, and like other land regions (3.5a), maximum near surface rain rates in the SEUS can exceed 150 mm hr^{-1}, with moderate maximum 40 dBZ heights, which is seen more rarely over oceans (3.5b).

3.2 SEUS comparisons of TRMM PR and WSR-88D retrievals

Comparisons will focus on three variables: reflectivity at 1.5-km altitude, rain rate at 1.5-km altitude, and the maximum height of the 40 dBZ echo in each column, for three datasets: TRMM-Ku, TRMM-S, and WSR-88D. The average 1.5-km altitude reflectivity for a given maximum 40 dBZ height is shown for each dataset in Figure 3.6. For maximum 40 dBZ heights below the melting level, assumed to be around 4-5 km, all three datasets vary similarly between 40 – 42 dBZ, with WSR-88D observing slightly higher 1.5-km altitude reflectivities than TRMM-Ku, and TRMM-S. However, for maximum 40 dBZ

echoes above 5-km altitude, differences occur between the WSR-88D and TRMM PR datasets. While reflectivity at 1.5 km increases with maximum 40 dBZ height at a similar rate across the three datasets, the WSR-88D reflectivities are approximately 2 dBZ higher than those of TRMM-Ku and TRMM-S. This offset forms very quickly between 5 and 7 km maximum 40 dBZ echo heights and then remains approximately constant with increasing maximum 40 dBZ height, with the conversion of TRMM-Ku to S-band having no effect. This result shows that 40 dBZ echoes extending into ice regions, indicative of graupel or hail presence, produce differences in TRMM PR and WSR-88D low level reflectivity that can impact rain rates retrieved by TRMM PR and WSR-88D.

WSR-88D data for this study comes from June, July, and August of 2013, while TRMM PR data comes from June-August of 2002-2013. To show that 2013 is not an anomalous year in our dataset, TRMM-Ku data for 2013 alone is shown in Figures 3.6 – 3.8 as a dashed line, which is consistent with the 12-year TRMM PR dataset (solid black) for maximum 40 dBZ echo heights below 10 km. The average 1.5-km altitude reflectivities with 40 dBZ echo heights greater than 10-km altitude, however, have large variability from bin to bin and large standard errors, indicative of small sample size in these maximum 40 dBZ echo height bins. Thus, differences between TRMM PR and WSR-88D for maximum 40 dBZ heights below 10 km appear to be robust, while above 10-km altitude, small 2013 sample sizes prevent assessment of robustness, although it is likely that 2013 WSR-88D statistics of 1.5-km reflectivity are not largely anomalous relative to 2002-2012, as they show a similar change with maximum 40 dBZ echo height as TRMM PR. Therefore, June-August 2013 is deemed to have sufficient and representative data to represent WSR-88D column statistics.

The average rainfall rate for a given reflectivity at 1.5-km altitude is shown in Figure 3.7. TRMM-Ku data for 2013 alone is shown as a black dashed line, indicating that 2013 again appears to be a non-anomalous year relative to the entire 12-year period from which TRMM PR statistics are accumulated. All three datasets have similar rain rates as a function of reflectivity below ~33 dBZ. However, above 33 dBZ, the rain rates as a function of reflectivity begin to diverge, with WSR-88D increasing the most quickly with reflectivity, followed by TRMM-S and finally TRMM-Ku. This results in an increasing gap between the calculated rain rate from WSR-88D and TRMM PR as 1.5-km altitude reflectivity increases. This gap is especially prevalent at 1.5-km altitude reflectivities of near 50 dBZ, with WSR-88D reaching 1.5-km rain rates of ~60 mm hr^{-1} while TRMM-Ku only reaches ~40 mm hr^{-1}. These differences can be attributed to the different methods that WSR-88D and TRMM PR use to calculate rain rate. Where the TRMM PR V7 2A25 algorithm uses Z-R relationships to calculate rain rates at all reflectivities (Iguchi et al. 2009), WSR-88D commonly uses R(KDP, ZDR) or R(KDP) relationships, where ZDR and KDP provide information on raindrop oblateness and number concentration that cannot be retrieved by TRMM PR. The differences in rain rate algorithms can also be seen once 1.5-km reflectivities reach 50 dBZ. Here, the increase in 1.5-km rain rates for WSR-88D changes slope while TRMM rain rates continue to increase exponentially with 1.5-km reflectivity. This change in the WSR-88D rain rate-reflectivity relationship is indicative of the algorithm's response to potential hail contamination and raindrop asphericity, which is further investigated in Chapter 4.

Figure 3.8 shows that WSR-88D rainfall rates at 1.5-km altitude are consistently higher than TRMM-S and TRMM-Ku for all maximum 40 dBZ echo heights. TRMM-Ku

and TRMM-S average rainfall rates show a slight upward trend for maximum 40 dBZ heights above the melting level, increasing from approximately 16 to 23 mm hr^{-1} between maximum 40 dBZ echo heights of 5 and 15 km. WSR-88D trends similarly to TRMM-S and TRMM-Ku below the melting level (comparable to Figure 3.6), however above 5-km altitude, the differences between TRMM PR and WSR-88D shown in Figures 3.6 and 3.7 compound to produce large differences in WSR-88D and TRMM PR mean rainfall rates as a function of maximum 40 dBZ height. Average rain rate increases from approximately 22 to 48 mm hr^{-1} as maximum 40 dBZ height increases from 4 to 14 km in the WSR-88D dataset, while TRMM-S only increases from approximately 15 to 24 mm hr^{-1} over the same range of maximum 40 dBZ heights. TRMM-Ku data from 2013 alone is shown as a black dashed line, again indicating that 2013 appears to be a non-anomalous year relative to the entire 12-year period from which TRMM PR statistics are accumulated.

Mean and median vertical reflectivity profiles for intervals of maximum 40 dBZ are shown in Figure 3.9. When the maximum 40 dBZ height is below the 5-km altitude (3.7a), there is good agreement in the average and median reflectivity profiles across the three datasets, consistent with how each of the datasets vary similarly below 5-km altitude in Figure 3.6. Once maximum 40 dBZ echo heights extend above 5 – 6 km, an offset between reflectivities in the different datasets appears in the rain region, with WSR-88D reflectivities higher than TRMM-Ku and TRMM-S reflectivities (consistent with Figure 3.6). Mean and median profiles for more convectively intense columns with maximum 40 dBZ heights between 10 – 15 km show a reflectivity offset of 5 dBZ and 2 dBZ in rain and ice regions, respectively, between WSR-88D and TRMM-S, with WSR-88D maintaining higher mean and median reflectivity values throughout most of the column. It is important

here to compare WSR-88D S-band retrieved reflectivities to TRMM-S calculated reflectivities as Mie scattering causes Ku-band reflectivities to be higher in rain regions and lower in ice regions when large hydrometeors are present in sufficient quantities. This is well illustrated in Figure 3.9c, where TRMM-Ku reflectivities are greater by approximately 2 dBZ than TRMM-S below 4 km, in the rain region, and are less than TRMM-S by approximately 1 dBZ between 5 – 10 km. The growth of this offset between WSR-88D and TRMM-S mean and median reflectivity profiles with increasing maximum 40 dBZ height indicates that TRMM PR 2A25 V7 retrievals may be becoming increasingly biased toward lower reflectivity and rain rate as graupel and hail content increase in the column.

Variable filled joint histograms further comparing these three variables across the datasets are shown in Figures 3.10 – 3.12. Figure 3.10 shows median 1.5-km altitude reflectivity as a function of the maximum 40 dBZ height and 1.5-km altitude rain rate. One of the notable differences between the WSR-88D dataset (3.10a) and the TRMM datasets (3.10b-c) is the shape of the joint distribution between maximum 40 dBZ height and 1.5-km altitude rain rate. All three datasets express their highest rain rates for maximum 40 dBZ heights near or just above the 0°C level, between 4 and 6 km altitude, which is consistent with Figure 3.4, however WSR-88D extends to higher rain rates (up to ~120 mm hr^{-1}) than TRMM PR (up to ~90 mm hr^{-1}), has higher rain rates for its most extreme maximum 40 dBZ height (30-45 mm hr^{-1} as compared to 0-20 mm hr^{-1}), and does not exhibit as steep of a drop in extreme maximum 40 dBZ heights as rain rates increase. The highest probability of extreme maximum 40 dBZ heights corresponding with relatively low rain rates at 1.5-km altitude is consistent with Figures 3.2 and 3.3, where the most

convectively intense columns do not correspond with the most intense rain rates. Because of their unique distribution shapes, the overlap fractions (Table 3.1) between the 90th, 95th, and 99th percentiles of the maximum 40 dBZ echo height and 1.5-km altitude rain rate vary, with WSR-88D having greater overlap fractions in all percentiles, ~50% higher overlap fraction than TRMM-S at the 95th percentile, where the overlap fractions of WSR-88D and TRMM-S are 0.23 and 0.16, respectively.

Consistent with TRMM, at a given rain rate under approximately 30 mm hr^{-1}, the WSR-88D reflectivity at 1.5-km altitude remains fairly constant with increasing maximum 40 dBZ echo height above the melting level, however a gradient appears as rain rates increase above 40 mm hr^{-1}. WSR-88D 1.5-km reflectivity continues to increase with increasing maximum 40 dBZ height for a given rain rate in this region, but for TRMM-Ku and TRMM-S datasets, 1.5-km reflectivity remains approximately constant with increasing maximum 40 dBZ echo heights above 7 km for a given rain rate. Additionally, Figure 3.10d shows that TRMM-S median 1.5-km reflectivities are consistently higher for a given maximum 40 dBZ height and 1.5-km rain rate than those from WSR-88D, with the largest magnitude difference (~6 – 8 dBZ greater) for rain rates above 60 mm hr^{-1} and maximum 40 dBZ heights above 5 km.

A similar comparison is made in Figure 3.11, this time with the relationship between maximum 40 dBZ height and 1.5-km altitude reflectivity color-filled with 1.5-km altitude rain rate. All three datasets exhibit a similar shape in their joint distributions. However, WSR-88D (3.9a) expresses a peak in the probability of extreme maximum 40 dBZ echo heights at higher 1.5-km altitude reflectivities, between 46 – 52 dBZ, than TRMM-Ku and TRMM-S (3.9b-c), which have highest probabilities between 40 and 50

dBZ. Because of this, the overlap fractions of extreme maximum 40 dBZ heights and extreme 1.5-km altitude reflectivities are once again higher for WSR-88D (35.25% overlap at the 95th percentile) than TRMM-Ku (11.18% overlap at the 95th percentile) and TRMM-S (5.51% overlap at the 95th percentile) (Table 3.2). For both TRMM-Ku and TRMM-S, rain rates at a given reflectivity are nearly constant or decrease as maximum 40 dBZ echo height increases, whereas they increase slightly within the WSR-88D dataset. With an exception for 1.5-km altitude reflectivities greater than 52 dBZ, the difference in rain rates (3.2d) between WSR-88D and the TRMM-S dataset reveals that WSR-88D has generally higher retrieved rain rates than TRMM-S for a given maximum 40 dBZ height and 1.5-km reflectivity, especially for maximum 40 dBZ heights greater than 5 km with 1.5-km reflectivities between 30 and 44 dBZ where WSR-88D rain rates are 30-90% higher.

The same comparison format is shown in Figure 3.12, with the relationship between 1.5-km altitude reflectivity and 1.5-km altitude rain rate color-filled with the median of the maximum 40 dBZ echo height in each bin. There exists a notable difference in the shape of the joint distributions between the WSR-88D dataset (3.12a) and the TRMM-Ku and TRMM-S (3.12b-c) datasets. While all three datasets exhibit an increase in rain rate with increasing reflectivity, WSR-88D has much more variable rain rates for a given reflectivity and a much wider range of reflectivities for a given rain rate than the TRMM-Ku and TRMM-S datasets. For example, for a 1.5-km rain rate of 20 mm hr^{-1}, WSR-88D 1.5-km reflectivity ranges from ~25 – 52 dBZ, as opposed to ~35 – 49 dBZ for both TRMM-Ku and TRMM-S. This results in TRMM-Ku and TRMM-S possessing higher overlap fractions between extreme low level rain rates and reflectivities, 0.67 and 0.66, respectively, at the 95th percentile, than WSR-88D, which has an overlap fraction of

approximately 0.23 at the 95th percentile (Table 3.3). The datasets also differ in their maximum 40 dBZ echo heights for a given reflectivity-rain rate bin. In the WSR-88D dataset, for a given 1.5-km altitude reflectivity, as rain rate increases, so does the maximum 40 dBZ echo height. However, in the TRMM and TRMM-S datasets, the opposite is true. Thus, in the TRMM datasets, relatively weak convection, as judged by the maximum height of the 40 dBZ echo, will have a higher mean 1.5-km altitude rain rate for a given 1.5 km reflectivity than relatively intense convection, while the opposite is true for WSR-88D. This contrast can be seen in the difference plot (3.12d), where WSR-88D maximum 40 dBZ heights for a given 1.5-km reflectivity are between 10 – 25% higher for more intense 1.5-km altitude rain rates and between 5 – 25% lower for weaker rain rates.

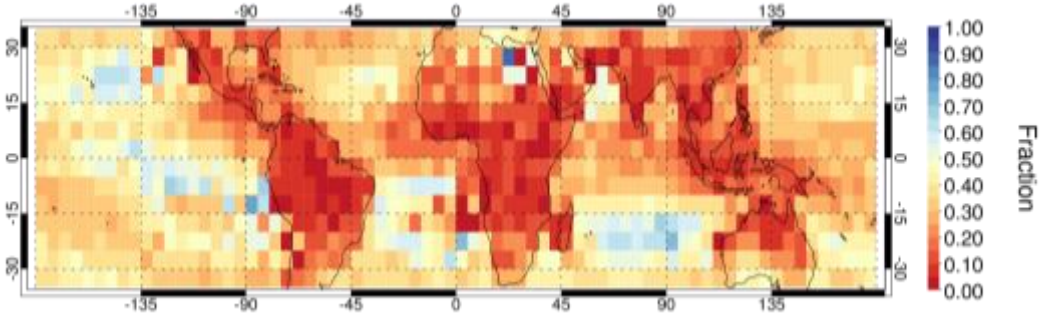

Figure 3.1 Fraction of the number of TRMM observed precipitation features in each 5° x 5° box, from 2002 – 2014, that contain a 99.5th percentile 40 dBZ echo height and a 99.5th percentile near-surface rainfall rate.

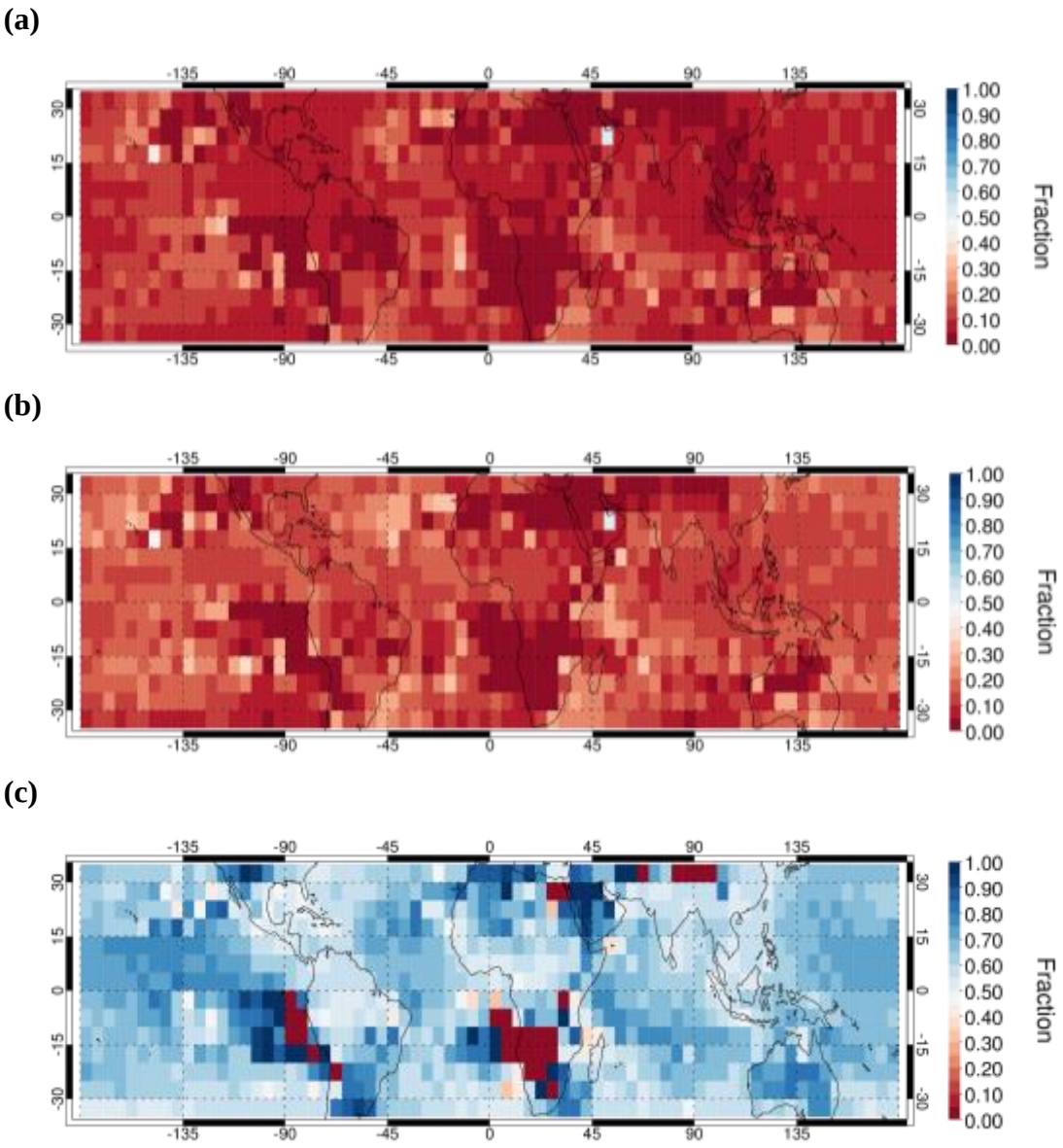

Figure 3.2 Fraction of TRMM observed columns in each 5° x 5° box, from 2002 – 2014, that contain 99.5th percentile (a) 40 dBZ echo heights and near-surface rainfall rates, (b) 40 dBZ echo heights and near-surface reflectivity, and (c) near-surface rainfall rates and near-surface reflectivity. This fraction is calculated using the same method as in Figure 3.1, for each comparison (a), (b), and (c) respectively.

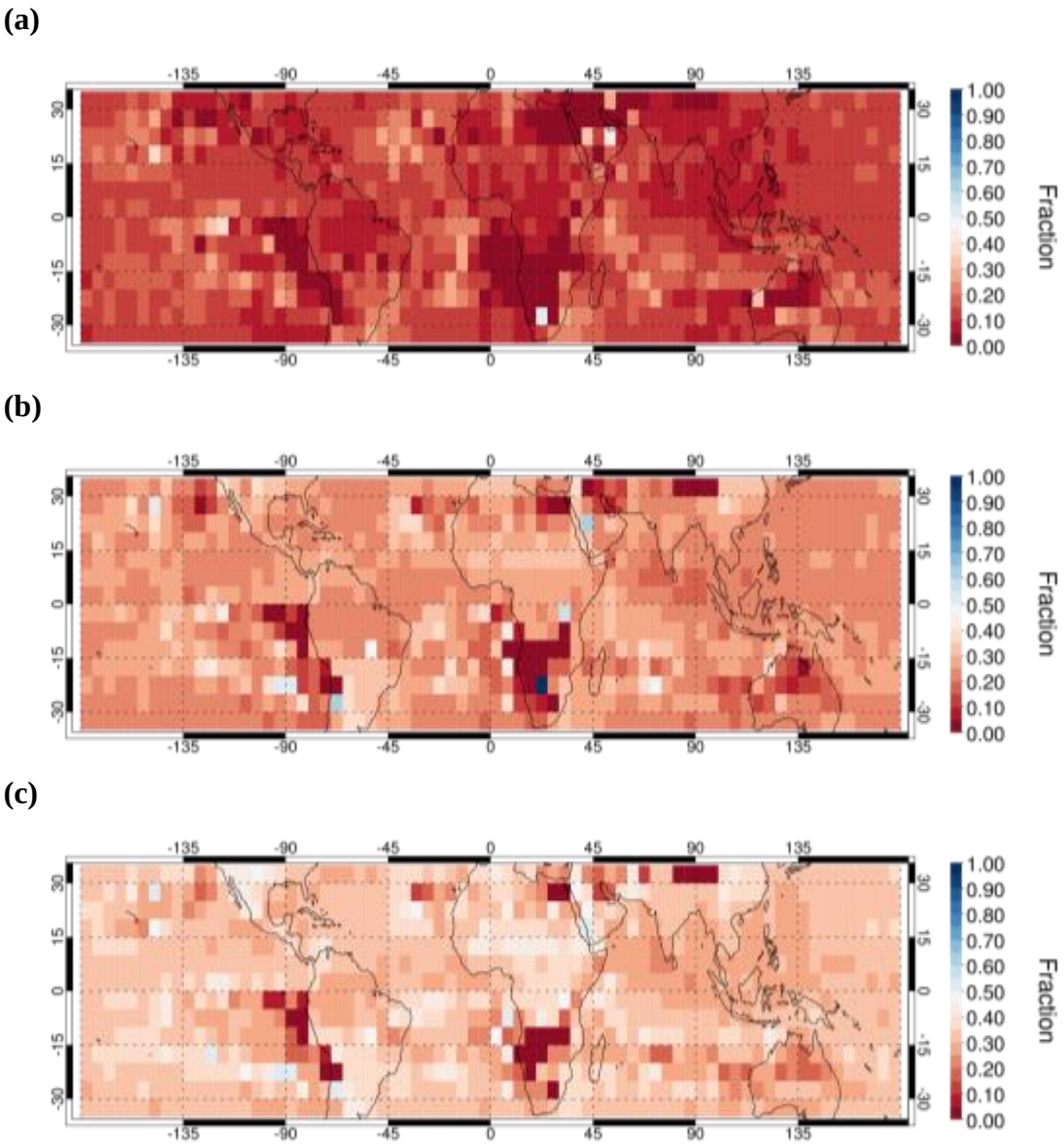

Figure 3.3 Fraction of TRMM observed columns in each 5° x 5° box, from 2002 – 2014, that contain maximum 40 dBZ echo heights and near-surface rainfall rates in the (a) 99th percentile, (b) 95th percentile, and (c) 90th percentile. This fraction is calculated using the same method as in Figure 3.1, for each comparison (a), (b), and (c) respectively.

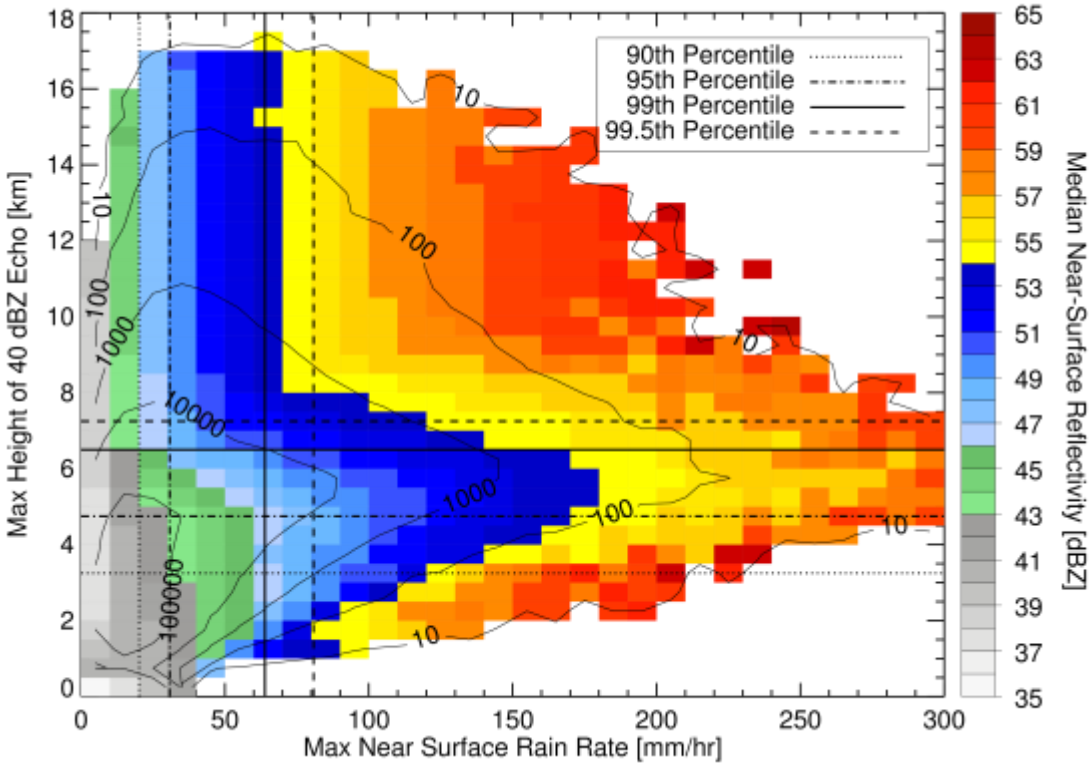

Figure 3.4 Joint histogram of maximum 40 dBZ echo height and near-surface rainfall rates, color filled with the median maximum near-surface reflectivity in each bin for observed TRMM PR PFs. The dashed black lines represent the 90th, 95th, 99th, and 99.5th percentiles of maximum near-surface rainfall rate and maximum 40 dBZ echo height, respectively. The sample size of PFs in the TRMM domain over 12 years (2002-2014) is 33,174,973.

(a)

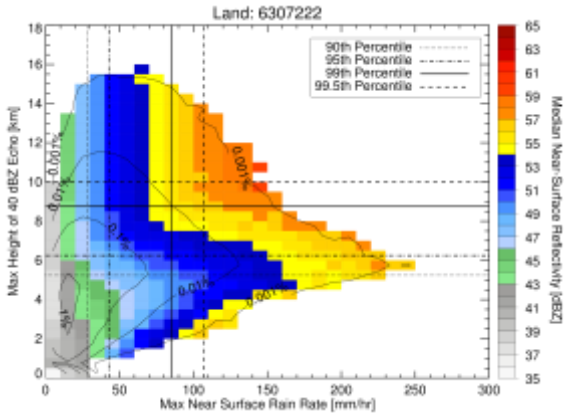

(b)

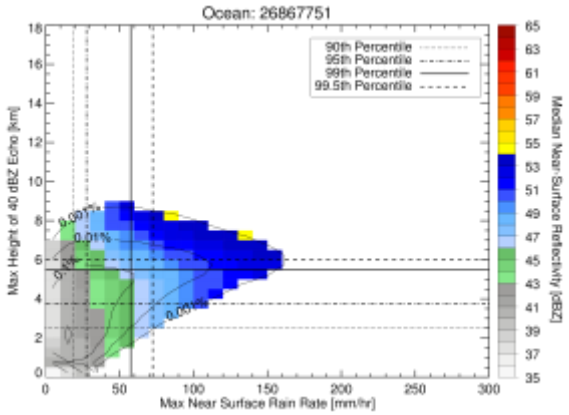

(c)

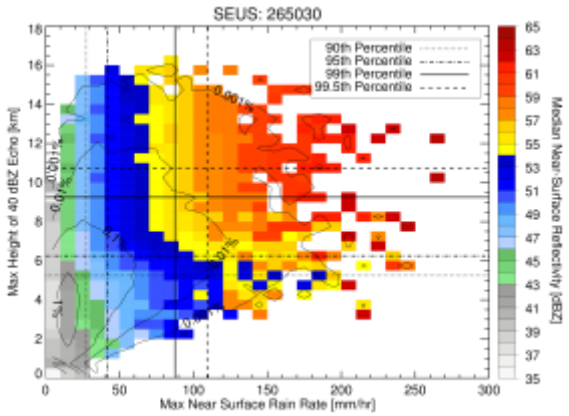

Figure 3.5 Joint probability density function of maximum 40 dBZ echo height and near-surface rainfall rates, color filled with the median maximum near-surface reflectivity in each bin for observed TRMM PR PFs over (a) land, (b) ocean, (c) the SEUS [25, 36, -80, -100. The sample sizes for each region are listed above each plot. The dashed black lines represent the 90th, 95th, 99th, and 99.5th percentiles of maximum near-surface rainfall rate and maximum 40 dBZ echo height, respectively.

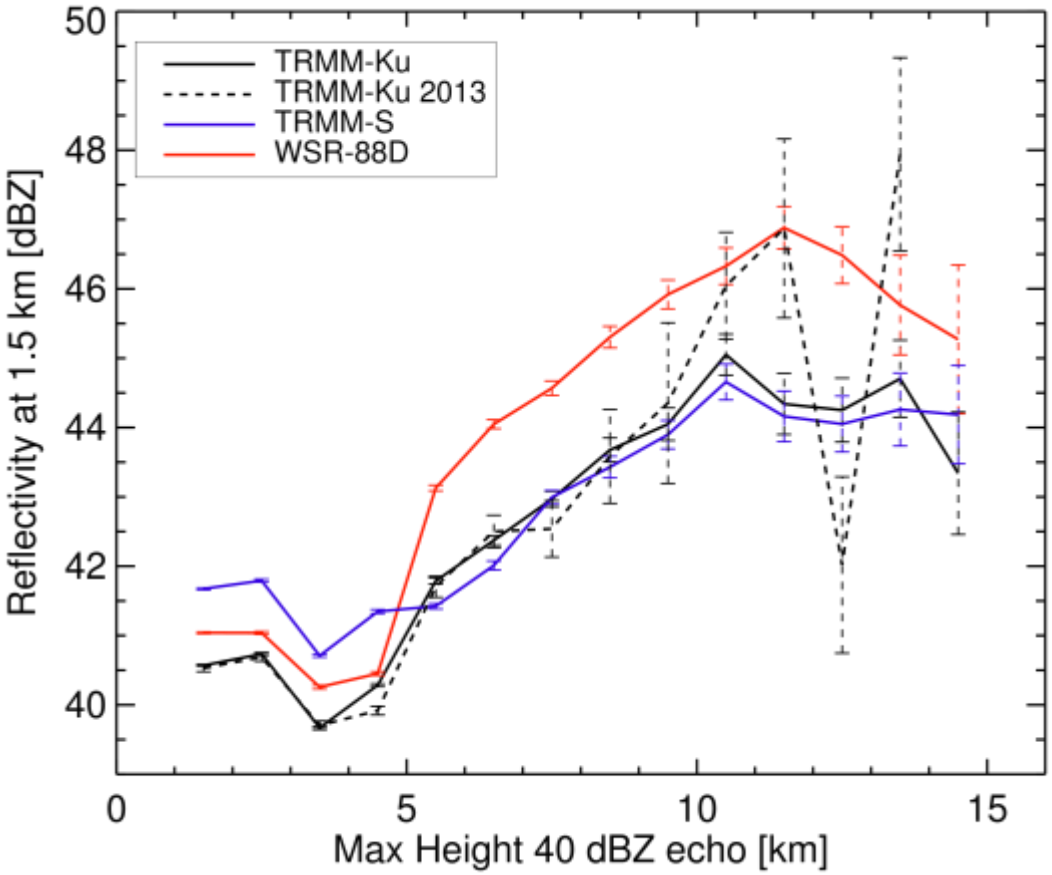

Figure 3.6 Solid lines represent the average reflectivity at 1.5 km for a given bin of maximum 40 dBZ echo height. TRMM data exclusively from 2013 is shown as a black dashed line. The vertical dashed lines represent the standard error in the mean for each dataset. A minimum 40 dBZ height threshold of 1.5 km is placed on the datasets, and the respective sample sizes for each dataset are: TRMM-Ku: 130,560; TRMM-S: 105,284; WSR-88D: 124,873; TRMM-Ku 2013: 12,708 columns.

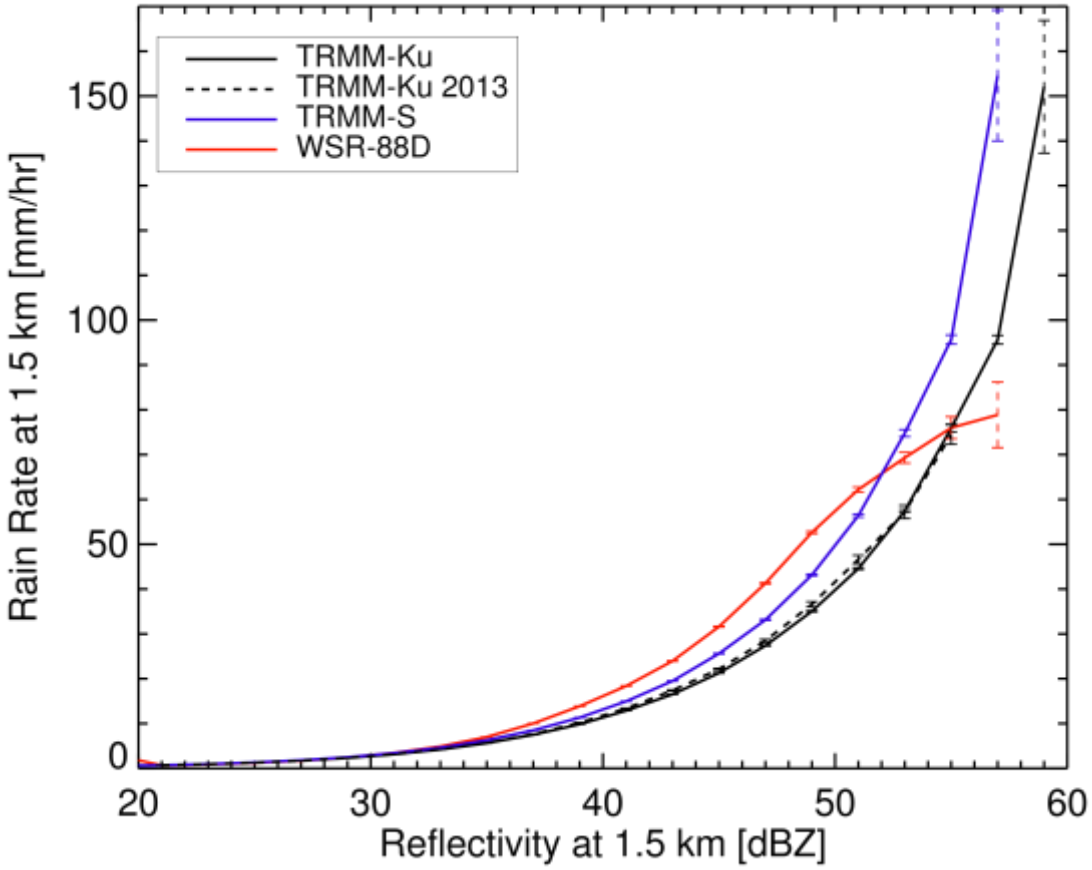

Figure 3.7 As in Figure 3.6, but for the average rainfall rate at 1.5 km for a given bin of reflectivity at 1.5 km. These samples are not restricted by a threshold on the maximum 40 dBZ height of a column. Therefore, for each dataset (TRMM-Ku, TRMM-S, and WSR-88D), the sample size is 700,594 columns. The TRMM-Ku 2013 dataset has 77,117 columns.

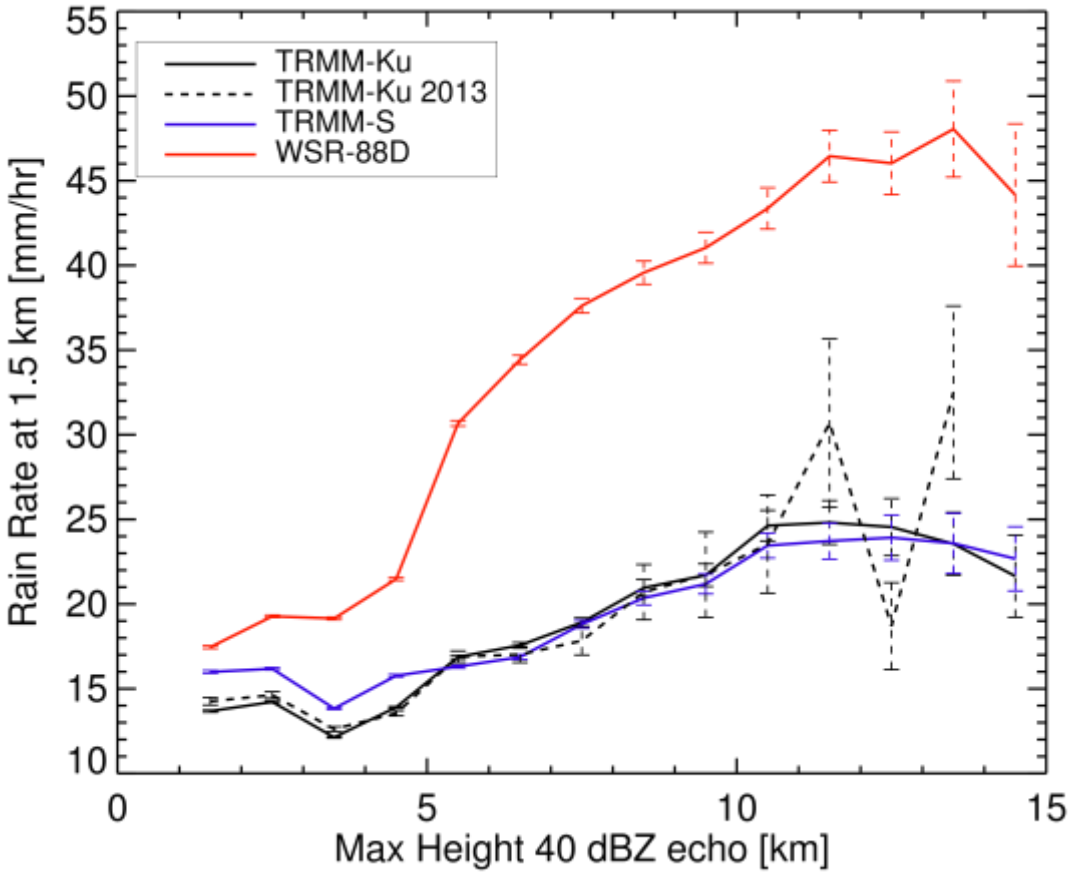

Figure 3.8 As in Figure 3.6, but for the average rainfall rate at 1.5 km for a given bin of maximum 40 dBZ echo height.

(a)

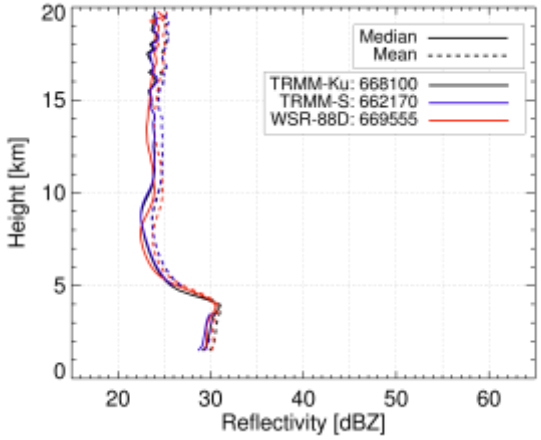

(b)

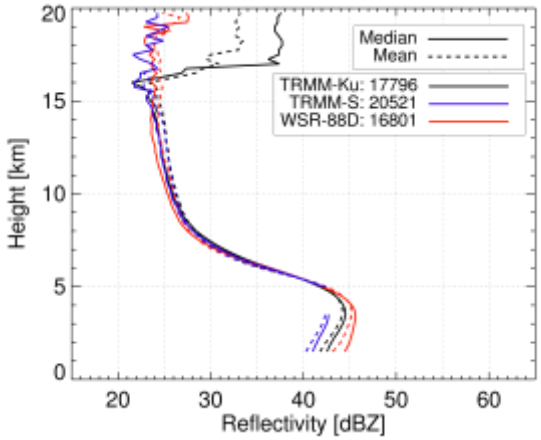

(c)

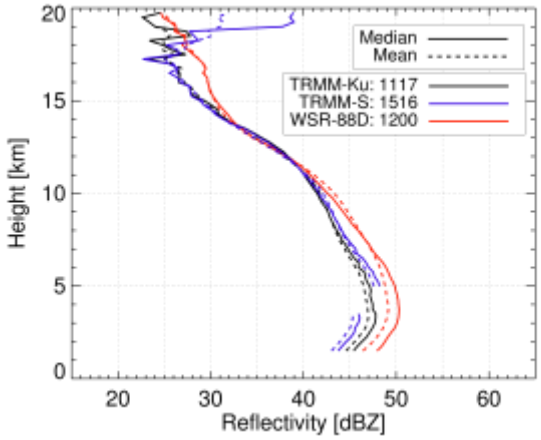

Figure 3.9 Mean and median vertical reflectivity profiles for systems with maximum 40 dBZ echo heights between (a) 0 – 5 km, (b) 5 – 6 km, and (c) 10 – 15 km for each of the three datasets. The respective sample size of each dataset is listed in each sub-figure (a-c).

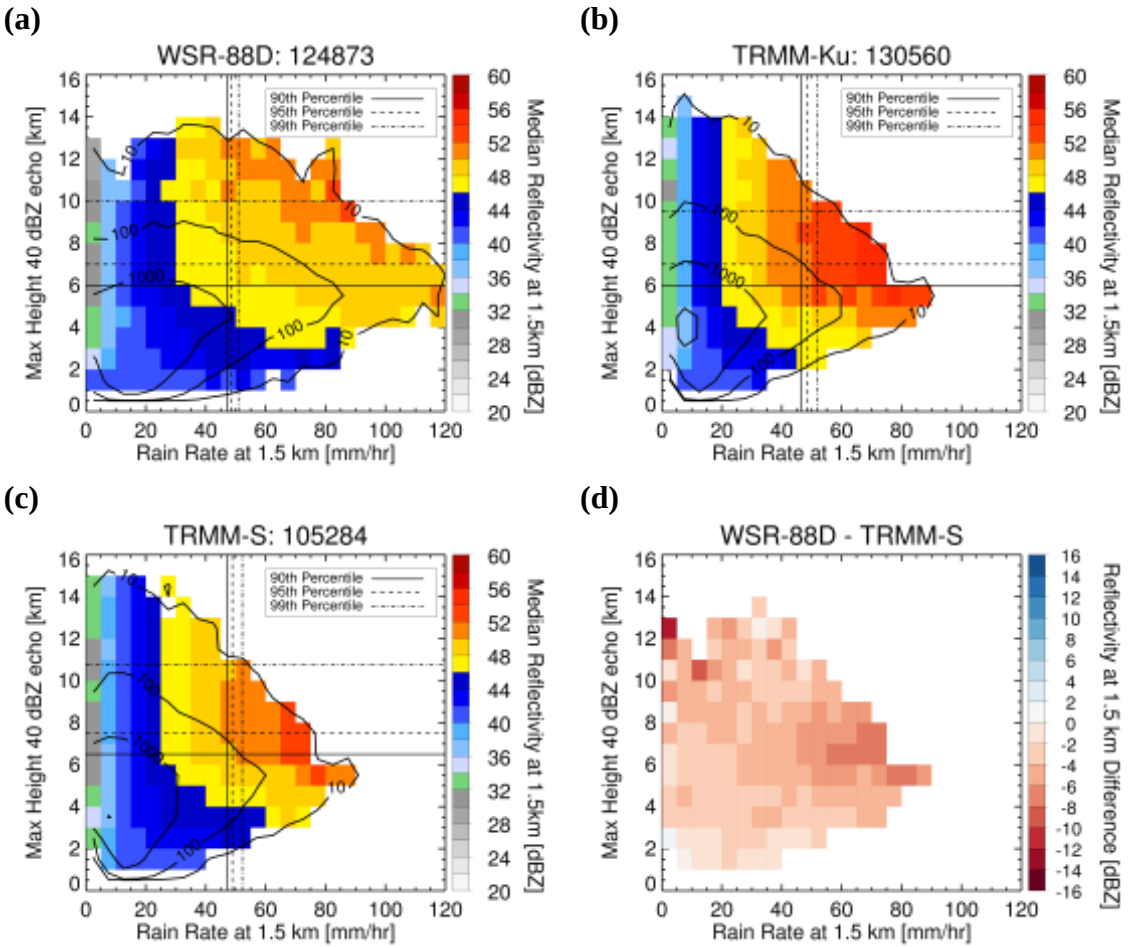

Figure 3.10 Joint histograms of maximum 40 dBZ echo height and rain rate at 1.5 km color filled with the median reflectivity at 1.5 km in each bin (a-c), and the difference in WSR-88D and TRMM-S reflectivity at 1.5 km (d). A minimum 40 dBZ height threshold of 1.5 km is placed on the datasets, and the respective sample size for each dataset is listed above each figure. Black overlaid lines represent the 90th, 95th, and 99th percentile thresholds for each variable.

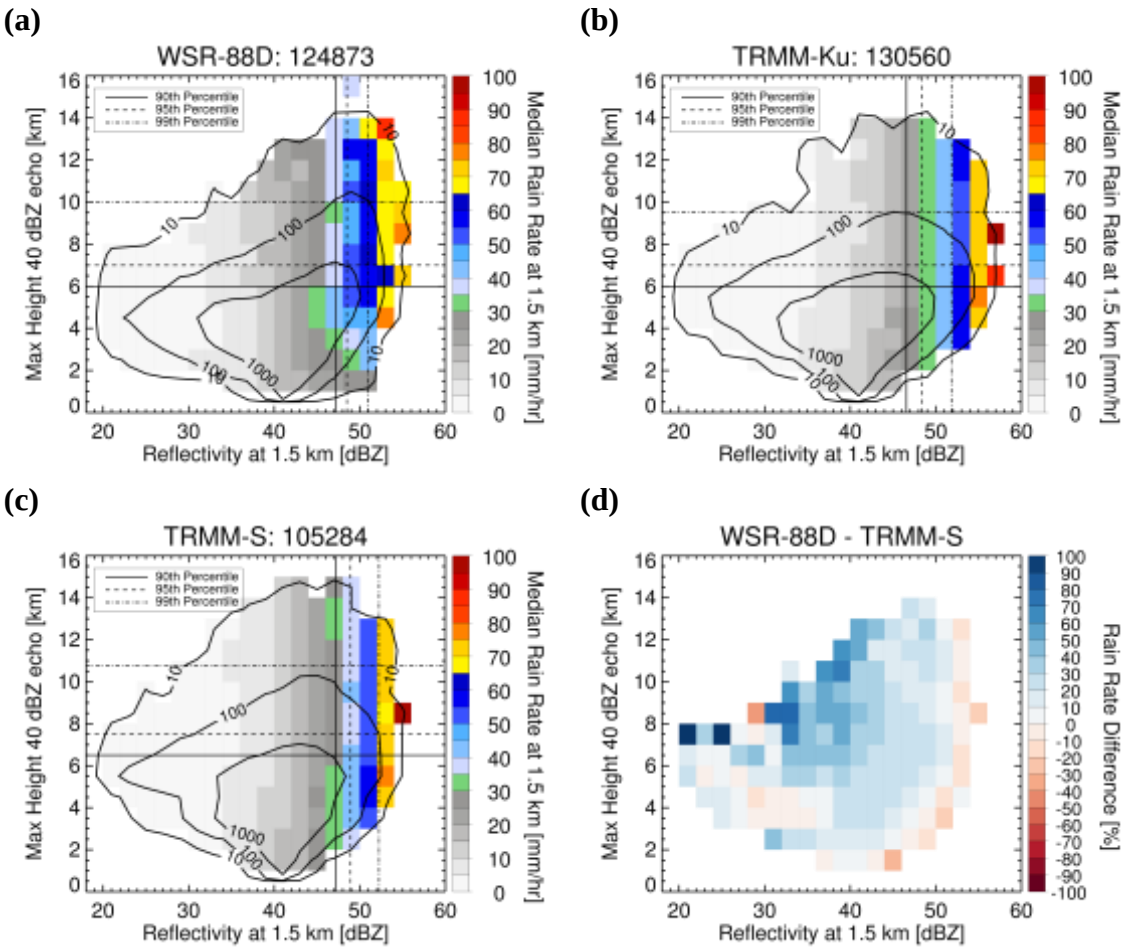

Figure 3.11 As in Figure 3.10, but for maximum 40 dBZ echo height and reflectivity at 1.5-km, color filled with median rain rate at 1.5 km in a-c and the difference in WSR-88D and TRMM-S rain rate in d.

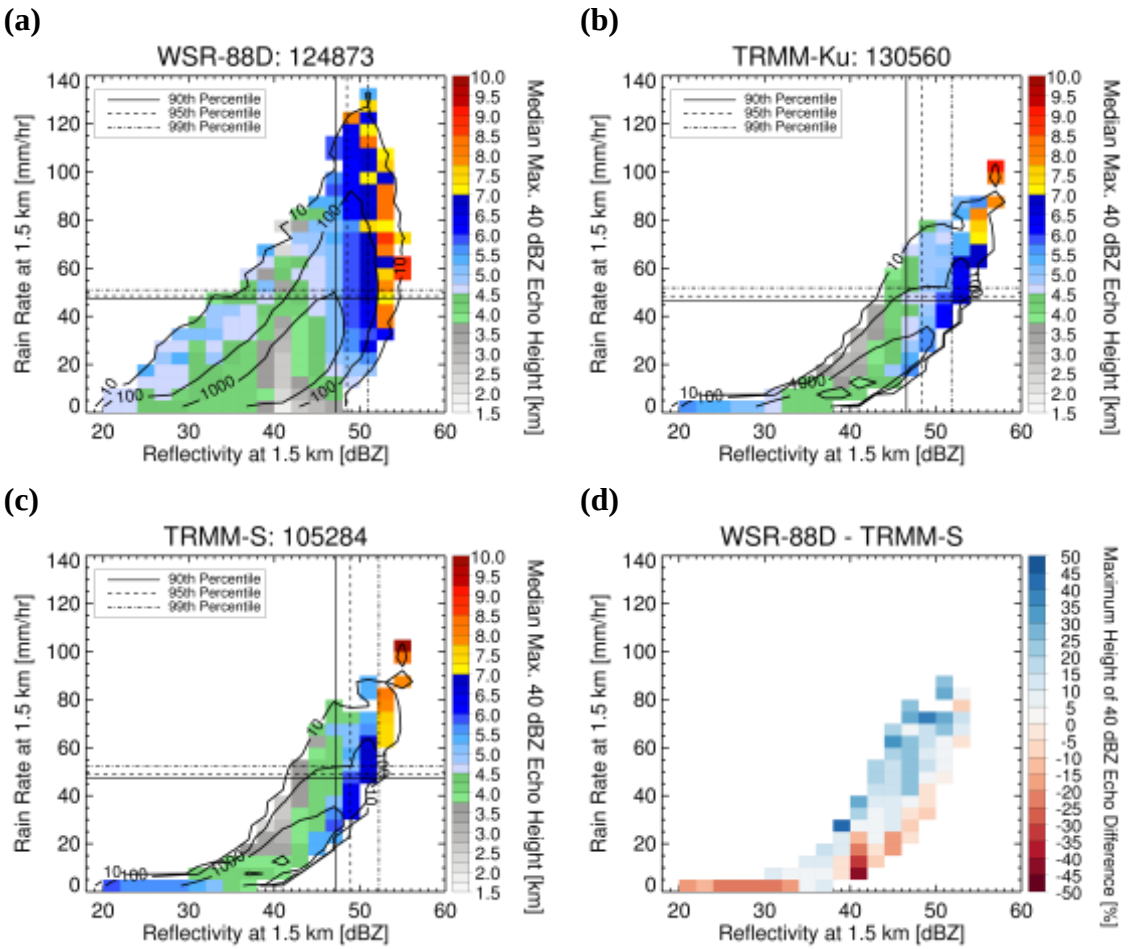

Figure 3.12 As in Figure 3.10, but for rain rate at 1.5 km and reflectivity at 1.5 km, color filled with median maximum 40 dBZ height in each bin in a-c and the difference of WSR-88D and TRMM-S maximum 40 dBZ height in d.

Table 3.1 Percentage of each dataset that exists in both the 90th, 95th, and 99th percentiles of maximum 40 dBZ heights and rain rates at 1.5 km, respectively, from Figure 3.8 (a-c).

Percentage of Overlap			
Percentile	WSR-88D	TRMM-S	TRMM-Ku
90th	34.2	22.84	24.67
95th	23.7	16.16	16.21
99th	9.69	7.41	8.35

Table 3.2 Percentage of each dataset that exists in both the 90th, 95th, and 99th percentiles of maximum 40 dBZ heights and reflectivity at 1.5 km, respectively, from Figure 3.9 (a-c).

Percentage of Overlap			
Percentile	WSR-88D	TRMM-S	TRMM-Ku
90th	44.66	21.22	33.98
95th	35.25	14.32	23.38
99th	19.78	5.51	11.18

Table 3.3 Percentage of each dataset that exists in both the 90th, 95th, and 99th percentiles of rain rates at 1.5 km and reflectivity at 1.5 km, respectively, from Figure 3.10 (a-c).

Percentage of Overlap			
Percentile	WSR-88D	TRMM-S	TRMM-Ku
90th	56.74	71.11	72.2
95th	46.14	66.37	67.22
99th	22.94	61.71	61.48

CHAPTER 4

PIA, KDP, ZDR, AND HAIL FRACTION ANALYSIS

4.1 TRMM PR PIA Analysis

PIA is considered one of the primary sources of uncertainty in the TRMM PR 2A25 rain rate algorithm (Iguchi 2009). Figure 4.1a-c shows mean PIA as a function of the three primary variables examined in Chapter 3: 1.5-km altitude reflectivity (4.1a), 1.5-km altitude rain rate (4.1b), and maximum height of the 40 dBZ echo (4.1c). As seen in 4.1a, mean PIA increases exponentially with increasing reflectivity, remaining less than 1 dB for 1.5 km reflectivities of 30 dBZ or lower, and increasing from approximately 4 to 10 dB for 1.5 km reflectivities of 40 to 50 dBZ. Mean PIA increases linearly with increasing 1.5 km rain rates (4.1b), however at rain rates greater than 80 mm hr^{-1}, the sample size per bin begins to decrease, as indicated by the increase in standard error of the mean, and therefore the PIA trend at these high rain rates is not as clear. Regardless of trend, PIA still exceeds 20 dB at these extreme 1.5 km rain rates. Mean PIA also increases with increasing maximum 40 dBZ echo heights (4.1c), which is consistent with Iguchi et al.'s (2009) results that attenuation in the 2A25 algorithm is especially problematic for extreme convection. The increase however, is not as large as was seen in the comparisons to 1.5-km reflectivities and rain rates, with the largest mean PIA values not exceeding 12 dB, despite maximum 40 dBZ echo heights reaching above 12 km. Figures 4.1a-c show that while extreme

convection is problematic for attenuation correction, extreme amounts of liquid cause the most attenuation, consistent with assumed attenuation coefficients for liquid and ice in V7 2A25 that vary by an order of magnitude.

This is further expressed in the PIA color-filled probability density functions shown in Figures 4.2a-c. In agreement with Figure 4.1a-b, the highest values of PIA are associated with the largest 1.5-km reflectivities (above ~50 dBZ) and rain rates (above ~50 – 60 mm hr^{-1}), as seen in Figure 4.2a-b, respectively, and highlighted in Figure 4.2c. Figure 4.2a-b also shows that for a given 1.5-km reflectivity, or a given 1.5-km rain rate, PIA increases with increasing maximum 40 dBZ height. For example, as seen in Figure 4.2b, at a 1.5-km rain rate of 60 mm hr^{-1} and a maximum 40 dBZ echo height of 4 km, the median PIA is around 12 dB, however for the same 1.5 km rain rate with a maximum 40 dBZ echo height of 8 km, the median PIA is ~20 dB. Despite this, the highest values of PIA exist for the highest rain rates, with the highest probability of maximum 40 dBZ heights between 5 – 9 km (4.2b) for these rain rates, indicating a stronger PIA dependency on the amount of rain present than on convective intensity. This is not all that surprising in that the specific attenuation is assumed to be an order of magnitude smaller for ice than for rain for a reflectivity of 40 dBZ in TRMM V7 2A25 (Iguchi et al. 2009). However, V7 2A25 assumes that rain exists below the melting level with a transition in the specific attenuation value from liquid values to ice values in a ~2.5 km layer above the melting level in convective regions. These assumptions can be potentially wrong in situations where the melting level is poorly estimated or when hail dominates the backscattered signal below the melting level, which can lead to low level reflectivity attenuation correction biases that negatively impact retrieved rain rates, possibly producing part of the differences with WSR-88D

results shown in Chapter 3.

4.2 WSR-88D Hail Fraction, KDP, and ZDR Analysis

Figure 4.3 shows the WSR-88D hail fraction as a function of 1.5-km altitude reflectivity, 1.5-km altitude rain rate, and maximum 40 dBZ echo height. Hail fraction is defined as the fraction of grid boxes at 1.125 km resolution within a 4.5 km footprint that have particle identifications indicative of rain mixed with hail or graupel. The average hail fraction increases with increasing 1.5-km reflectivity (4.3a), and experiences a significant rate of increase for 1.5-km reflectivities above 50 dBZ, growing from approximately 0.3 to 0.7. This is expected as hail particles can exceed raindrops in size and thus produce higher reflectivity values. As 1.5-km rain rates increase, however, hail fraction remains around 0.2 (4.3b). As depicted in the CSU-HIDRO algorithm (Cifelli et al. 2011) summarized in Figure 2.1, rain rates are not calculated for columns that have a particle identification of hail or in some cases, a hail-rain mix, which may restrict the hail fraction from growing too much with increasing rainfall rate. Figure 4.3c shows that when maximum 40 dBZ echo heights are below the melting level, assumed to be between 4 -5 km, hail fraction remains approximately constant at 0.1, however as heights enter the ice region, hail fraction increases from 0.1 to ~0.45 as maximum 40 dBZ echo heights increase to 14 km. This is anticipated as more convectively intense systems are expected to have a higher probability of producing significant amounts of hail.

Joint histograms of 1.5-km rain rate, 1.5-km reflectivity, and maximum 40 dBZ echo height are filled with hail fraction in Figure 4.4a-c. In Figure 4.4a, regions of higher hail fractions are collocated with the greatest 1.5-km reflectivities (greater than 50 dBZ)

and the highest maximum 40 dBZ heights (greater than 8 km). This is supported by the results in Figures 4.3a and 4.3c, which show that hail fraction increases with increasing 1.5-km reflectivity and maximum 40 dBZ height respectively. The hail fraction in the maximum 40 dBZ height and 1.5-km rain rate joint histogram (4.4b) is telling. First, hail fraction increases from approximately 0.3 to 0.6 with increasing maximum 40 dBZ height above 6 km for a given 1.5-km rain rate. This result complements what is shown in Figure 4.3c, as systems with taller maximum 40 dBZ heights are more convectively intense, and thus more capable of producing significant amounts of hail and/or graupel. TRMM PR observed columns in Figure 4.2b with similar characteristics to those with high hail fractions from Figure 4.4b, (1.5-km rain rates between 20 – 60 mm hr^{-1}, and maximum 40 dBZ heights above 8 km) are not areas of extreme PIA, however they still reach significant values of up to 15 dB. Hail that is reaching low levels and producing a significant hail fraction in WSR-88D retrievals is also misidentified as liquid in 2A25, which could also cause a bias in the way that PIA is distributed vertically to give an attenuation corrected reflectivity profile, since in the 2A25 algorithm, ice is assumed to attenuate at an order of magnitude smaller than liquid for a given significant reflectivities (Iguchi et al. 2009).

Specific differential phase (KDP) and differential reflectivity (ZDR) are used to investigate characteristics in raindrop oblateness and number concentration that can impact the relationship between reflectivity and rain rate assumed in TRMM 2A25. Figure 4.5 shows KDP (a-b) and ZDR (c-d) relationships as they relate to 1.5-km reflectivity and rain rate. KDP increases linearly with 1.5-km rain rate, from 0° km^{-1}, when it is not raining, to 2.5° km^{-1} at rain rates of 120 mm hr^{-1} (4.5b). This is expected in that KDP is greater in heavy rain due to large concentrations of moderate to large raindrops that are oblate and

cause different propagation speeds of horizontal and vertical polarized signals. Mean rain rate shares an exponential relationship with reflectivity, as shown in Figure 3.7, and mean KDP also expresses an exponential relationship with reflectivity (4.5a), while mean ZDR increases with increasing reflectivity, from approximately 0.5 dB at reflectivities of 20 dBZ to 2 dB at reflectivities of 50 dBZ (4.5c). At approximately 58 dBZ, there is a sharp drop to near -3 in the average ZDR, however the median value is just above 0. Given the limited sample size at these high reflectivity values, these values are not robust and may be responding to situations that failed to be removed from the analysis in which hail or non-meteorological signals are dominating the reflectivity rather than rain. However, mean ZDR increases from 0.7 to 1.6 dB with 1.5-km rain rate only until about 40 mm hr^{-1} (4.5d), meaning oblate raindrops are becoming more common with increasing rain rate, but it remains approximately constant around 1.5 dB or even decreases slightly to 1.4 dB as rain rates increase beyond 40 mm hr^{-1}.

Figures 4.6 and 4.7 revisit the WSR-88D joint histograms between the three primary variables of interest, with color filled median KDP and ZDR, for each bin respectively. Figure 4.6 shows that for a given 1.5-km reflectivity, KDP does not express sensitivity to the maximum height of the 40 dBZ echo (4.6a). For example, at 1.5-km reflectivities of approximately 45 dBZ, KDP remains approximately 0.5 – 0.6° km^{-1}, regardless of the maximum height of the 40 dBZ echo. However, for 1.5-km rain rates above 30 mm hr^{-1}, KDP increases for a given 1.5-km rain rate as maximum 40 dBZ height increases, where a 1.5-km rain rate of 80 mm hr^{-1} has a KDP of 1.5° km^{-1} and 2° km^{-1} when maximum 40 dBZ echo heights are 4 and 9 km, respectively (4.6b). The largest values of KDP are associated with the areas of highest rain rate in all joint PDFs (4.6a-c). Superior

rain rate information is provided by KDP in situations of heavy rain or hail mixed with rain (Cifelli et al. 2011), but this information was not retrievable by TRMM PR, and these situations are also ones in which PIA is significant, meaning phase and drop size distribution assumptions used in the 2A25 retrieval of rain rate for these situations may be contributing to near surface reflectivity and rain rate biases.

This issue is further expressed through Figure 4.7, where regions of positive ZDR are responding to asphericity in the drop size distribution at 1.5-km altitude. Figure 4.7a shows that for all columns with maximum 40 dBZ echo heights above 8 km, median ZDR varies from 1.5 to 3 dB. Strongly positive values of ZDR also exist for lesser maximum 40 dBZ echo heights where the reflectivity at 1.5-km altitude is greater than 50 dBZ. These regions indicate situations with large, oblate raindrops that TRMM is not able to accurately detect, therefore restricting a more accurate rain rate retrieval for these high reflectivity situations. From Figure 4.4b, it is known that the area of strongly positive ZDR in Figure 4.7b coincides with an area of significant hail fraction. Hail tends to be spherical in a mean sense as it tumbles when it falls, and thus ZDR typically retrieves a value near 0 for hail. A strongly positive ZDR in addition to high hail fractions at 1.5 km therefore indicates significant asphericity in the particles contributing to the backscattered radiation, likely indicating regions that commonly have hail mixed with large raindrops that further violate assumptions made in the drop size distributions for the TRMM 2A25 V7 algorithm, therefore impacting attenuation correction. Areas of strongly positive ZDR in Figures 4.7a-b appear in Figure 4.7c as strongly positive ZDR on both the right and left flanks of the PDF. Interestingly, for a given 1.5-km reflectivity greater than 38 dBZ, ZDR decreases with increasing 1.5-km rain rates from ~2.5 dB to ~1.1 dB at a 1.5-km reflectivity of ~45

dBZ, but Figure 4.6c shows an increase in KDP from 0° km^{-1} to ~1.8° km^{-1} at a 1.5-km reflectivity of ~45 dBZ in this same region. The increase in KDP implies that the number concentration of oblate raindrops is increasing with rain rate, causing a larger differential phase shift, while a ZDR decrease indicates that this increase in number concentration is likely from moderate sized, slightly oblate raindrops with a decrease in large, very oblate raindrops that were causing larger ZDR values at the lower rain rates. The opposite is true when 1.5-km reflectivity is less than 38 dBZ, when ZDR is strongly positive but corresponds with low KDP (4.6c), indicating a small concentration of oblate raindrops that cause only a slight change in differential phase, but a significant change in differential reflectivity.

(a)

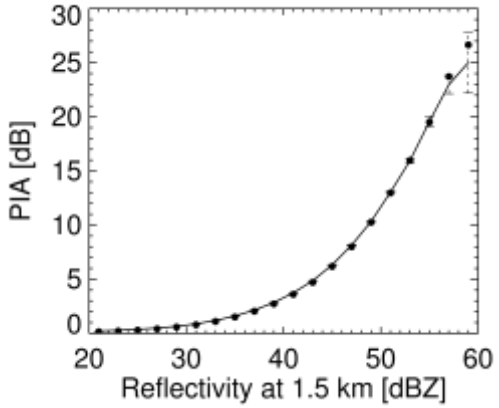

(b)

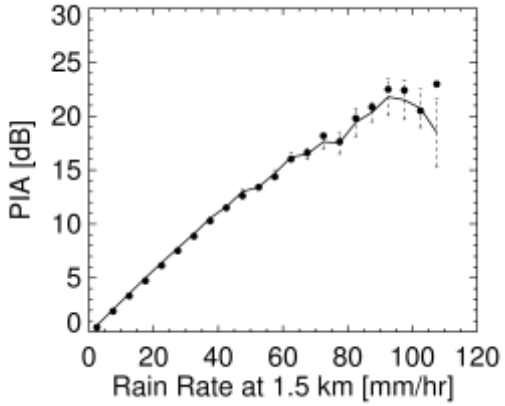

(c)

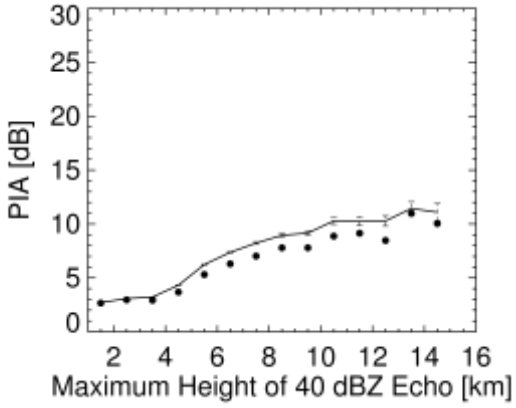

Figure 4.1 TRMM-Ku PIA relationships. The solid line represents the average PIA for a given bin of reflectivity at 1.5 km (a), rain rate at 1.5 km (b), and maximum 40 dBZ echo height (c). The median PIA for a given bin is expressed by the solid dot. The vertical dashed lines represent the standard error in the mean. A minimum 40 dBZ height threshold of 1.5 km is placed on the datasets and the respective sample size for these figures is 130,560 columns.

(a)

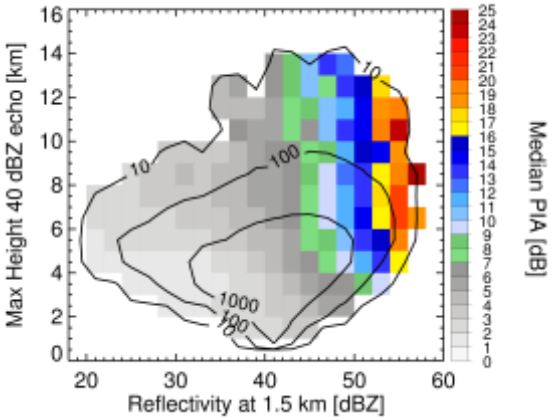

(b)

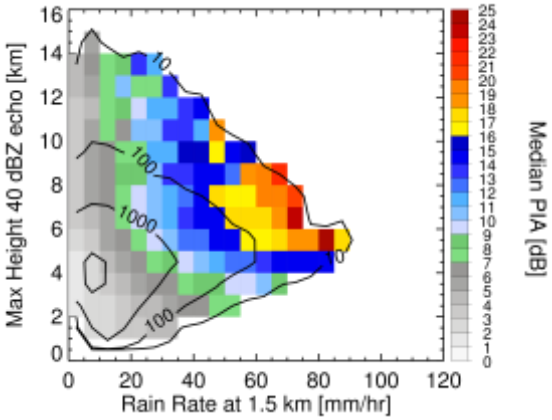

(c)

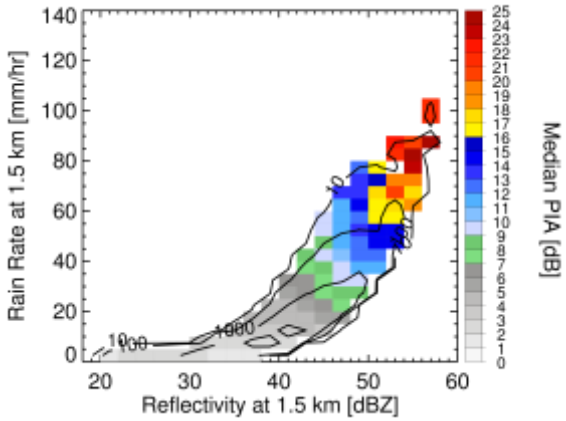

Figure 4.2 Joint histograms of TRMM-Ku maximum 40 dBZ echo height and reflectivity at 1.5 km (a), maximum 40 dBZ echo height and rain rate at 1.5 km (b), and rain rate at 1.5 km and reflectivity at 1.5 km (c), all color-filled with the median PIA in each bin. A minimum 40 dBZ height threshold of 1.5 km is placed on the datasets and the respective sample size for these figures is 130,560 columns.

(a)

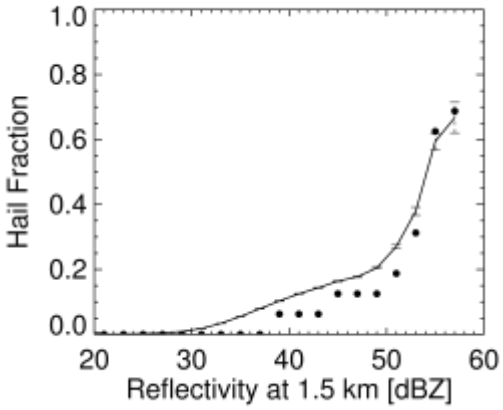

(b)

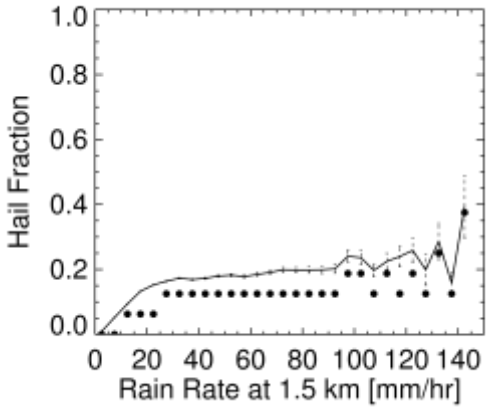

(c)

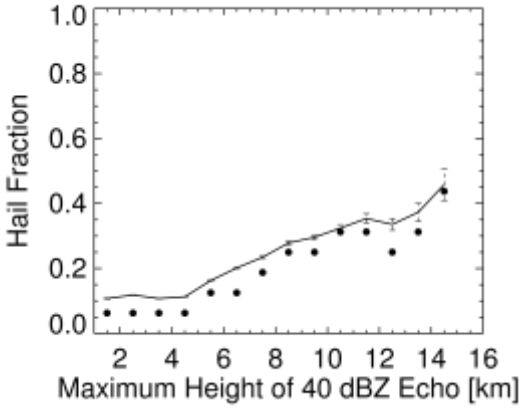

Figure 4.3 WSR-88D hail fraction relationships. The solid line represents the average hail fraction for a given bin of reflectivity at 1.5 km (a), rain rate at 1.5 km (b), and maximum 40 dBZ echo height (c). The median hail fraction for a given bin is expressed by the solid dot. The vertical dashed lines represent the standard error in the mean. A minimum 40 dBZ height threshold of 1.5 km is placed on the datasets and the respective sample size for these figures is 124,873 columns.

(a)

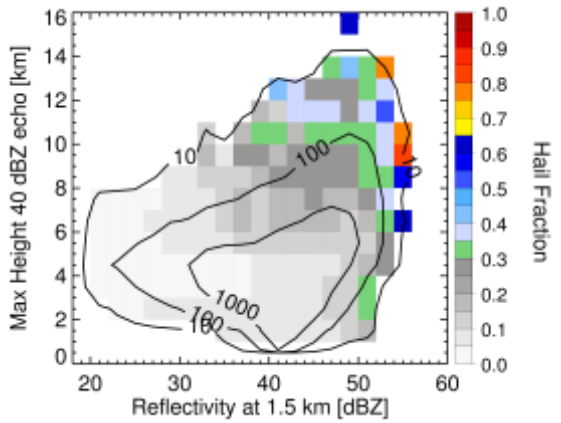

(b)

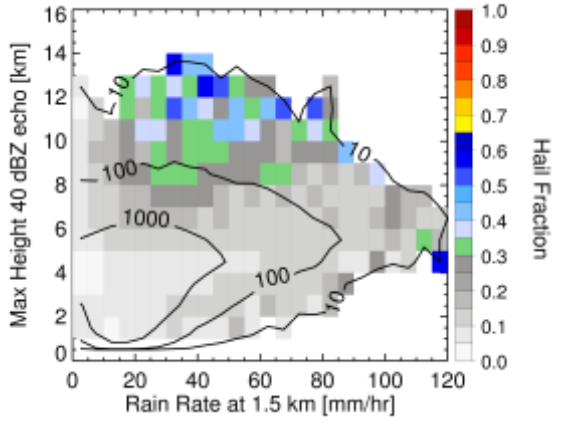

(c)

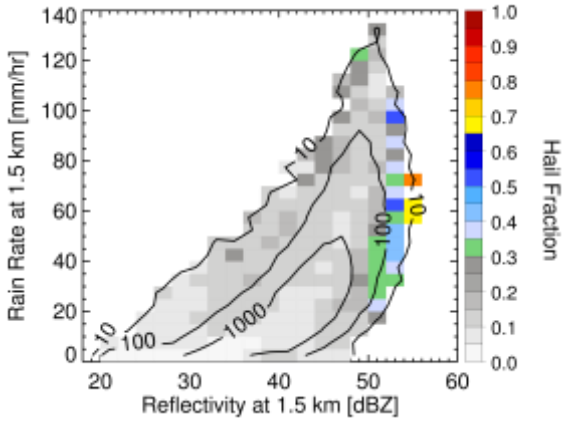

Figure 4.4 Joint histograms of WSR-88D maximum 40 dBZ echo height and reflectivity at 1.5 km (a), maximum 40 dBZ echo height and rain rate at 1.5 km (b), and rain rate at 1.5 km and reflectivity at 1.5 km (c), all color-filled with the median hail fraction in each bin. A minimum 40 dBZ height threshold of 1.5 km is placed on the datasets and the respective sample size for these figures is 124,873 columns.

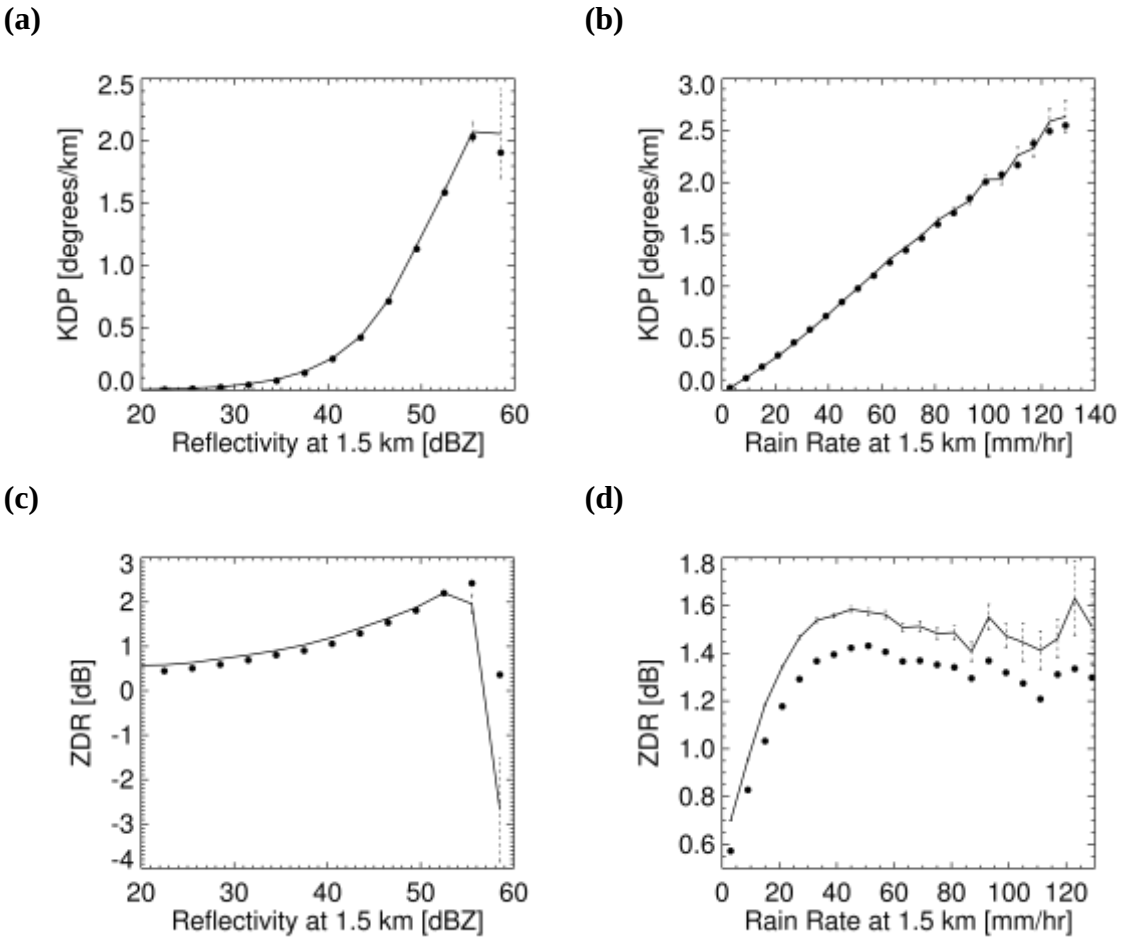

Figure 4.5 WSR-88D KDP and ZDR relationships. The solid line represents the average value of KDP (a-b) and ZDR (c-d) for a given reflectivity at 1.5 km (a, c) and rain rate at 1.5 km (b, d) bin. Median values of KDP and ZDR are given by black dots, with the vertical dashed lines representing the standard error in the mean. This comparison used the entire sample; 700,594 columns.

(a)

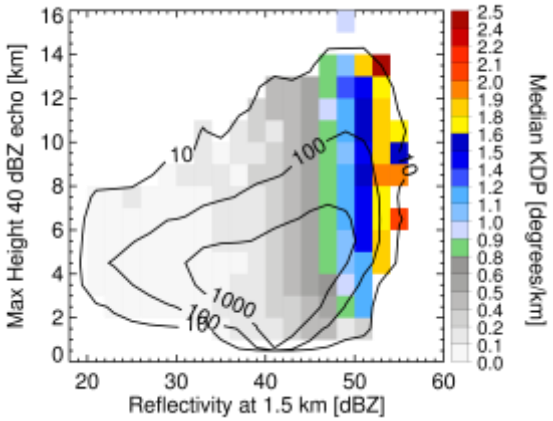

(b)

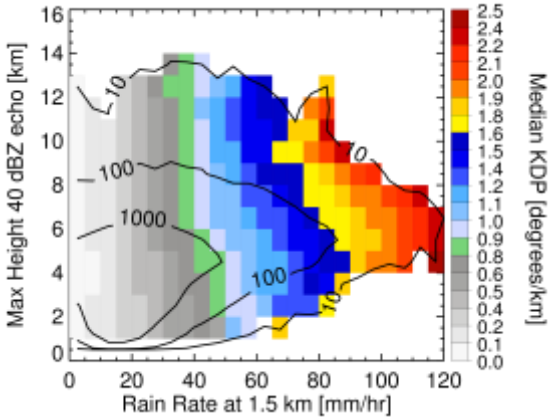

(c)

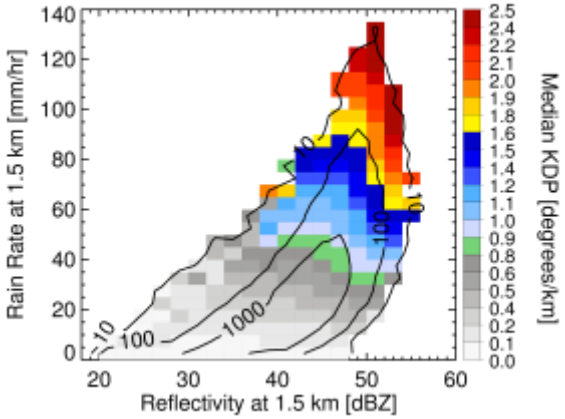

Figure 4.6 Joint histograms of WSR-88D maximum 40 dBZ echo height and reflectivity at 1.5 km (a), maximum 40 dBZ echo height and rain rate at 1.5 km (b), and rain rate at 1.5 km and reflectivity at 1.5 km (c), all color-filled with the median KDP in each bin. A minimum 40 dBZ height threshold of 1.5 km is placed on the datasets and the respective sample size for these figures is 124,873 columns.

(a)

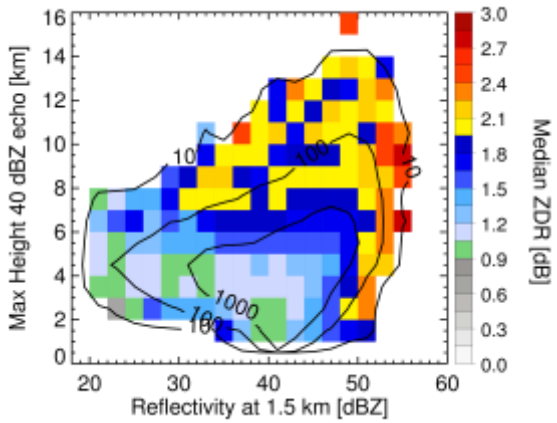

(b)

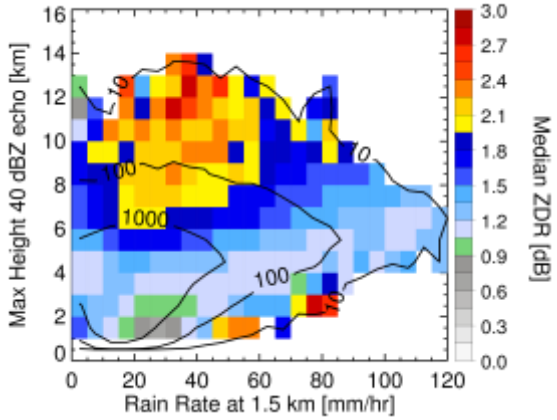

(c)

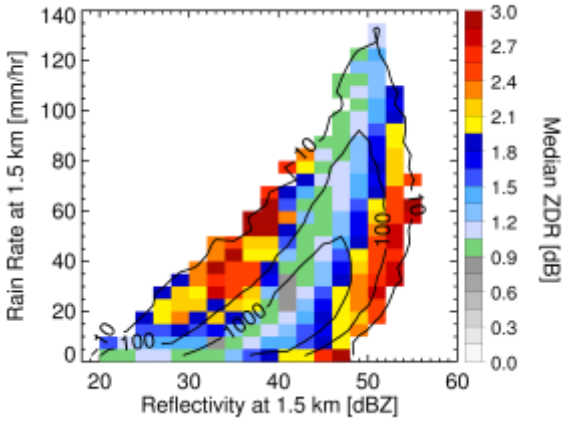

Figure 4.7 Joint histograms of WSR-88D maximum 40 dBZ echo height and reflectivity at 1.5 km (a), maximum 40 dBZ echo height and rain rate at 1.5 km (b), and rain rate at 1.5 km and reflectivity at 1.5 km (c), all color-filled with the median ZDR in each bin. A minimum 40 dBZ height threshold of 1.5 km is placed on the datasets and the respective sample size for these figures is 124,873 columns.

CHAPTER 5

CONCLUSIONS

5.1 Summary

The TRMM satellite has produced an invaluable 17-year dataset of precipitation retrievals over the tropics and subtropics, and in this study, the TRMM PR 2A25 V7 retrievals are used to examine the overlap between extreme rain rates and extreme convective intensities. While it is often assumed that extreme convectively intense precipitation features usually produce extreme rainfall rates, Hamada et al. (2015) showed via the TRMM PR 2A25 V7 dataset that this is frequently not the case and that extreme rain rates are commonly found in convection of moderate strength. It is well known, however, that intense convection poses special difficulties for the TRMM PR operating at Ku-band because of its susceptibility to attenuation, especially by liquid and/or partially melted hydrometeors. This is a serious issue for two reasons: (1) estimates of PIA are subject to significant error, and (2) distributing the PIA as a function of height involves assumptions that may produce reflectivity and rain rate profile biases in intense, deep convection. It is therefore important to quantify potential biases in TRMM PR retrieved reflectivity profiles and low level rain rates that may result from TRMM PR attenuation correction and Z-R relationship assumptions that are inappropriate for intense, deep

convection. This is accomplished by comparing TRMM PR retrievals against S-band observations with minimal attenuation from NOAA WSR-88D radars.

This study uses 13 years (2002-2014) of June - August TRMM PR 2A25 V7 data with a focus on three variables: 1.5-km altitude reflectivity, 1.5-km altitude rainfall rate, and the maximum height of the 40 dBZ echo, which is used as a proxy for convective intensity. These same three variables are determined for hourly WSR-88D observations in June-August 2013 for 28 radars over the southeastern United States where the CSU-HIDRO algorithm is used to calculate rainfall rates from Z, ZDR, KDP, and PID. WSR-88D observations are gridded to a horizontal resolution of 1.125-km and then degraded to a 4.5-km horizontal resolution to match that of the TRMM PR post-orbital boost. Because TRMM's orbit results in a high sample rate at the northern edge of the domain, and because WSR-88Ds are not evenly spaced geographically, the two datasets are limited to full columns of data covering 1.5 to 15 km altitudes within 80 km of each of the 28 WSR-88D radars, and then their sample sizes are matched by randomly sampling the larger of the two datasets down to the size of the limiting dataset. Additionally, a third dataset is created by converting TRMM Ku-band measurements to S-band approximations, allowing for a more direct comparison of TRMM PR reflectivity retrievals with WSR-88D observations. For this study, relationships between 1.5-km altitude rain rates, 1.5-km altitude reflectivities, and maximum 40 dBZ heights for the 3 datasets (WSR-88D, TRMM-Ku, and TRMM-S) are analyzed for individual columns rather than entire contiguous precipitation features.

TRMM PR retrievals across the tropics and subtropics show that the most extreme near-surface rain rates have the highest probability of a maximum 40 dBZ echo height that exists near or just above the melting level (~5 km). The overlap of the 99^{th} percentiles of

1.5-km rainfall rate and maximum 40 dBZ height is less than 20% in all regions with significant rainfall. This agrees well with the low overlap fraction from the precipitation feature perspective, indicating that both precipitation features and individual data columns with the tallest 40 dBZ echo heights are rarely the features with the highest near-surface rainfall rates. A similar result is found in the overlap fraction of the 99th percentiles of 1.5-km altitude reflectivity and maximum 40 dBZ height, which is expected since rain rate is calculated from reflectivity via Z-R relationships in the 2A25 algorithm. It therefore also follows that overlap fractions between the 99th percentiles of 1.5-km reflectivity and 1.5-km rainfall rate are large over both ocean and land throughout the tropics and subtropics. Results also show that the southeastern United States has overlap fractions that appear to be fairly representative of other land regions across the tropics and subtropics. Specifically, this region often exhibits extreme maximum 40 dBZ heights with limited rain rates, and also extreme rain rates with limited maximum 40 dBZ heights, making it a good region for evaluating the robustness of overlap fractions derived from TRMM PR.

Analysis of 1.5-km altitude reflectivity as a function of maximum 40 dBZ echo height retrieved by WSR-88D, TRMM-Ku, and TRMM-S over the southeastern United States shows that when maximum 40 dBZ heights extend into regions likely containing ice, indicative of the presence of graupel or hail, WSR-88D retrieves a 1.5-km altitude reflectivity that is ~2 dBZ higher than TRMM-Ku and TRMM-S for a given maximum 40 dBZ height. Mean 1.5-km rain rates retrieved by TRMM PR and WSR-88D diverge when reflectivity exceeds ~33 dBZ, with the WSR-88D algorithm yielding significantly higher rain rates for a given reflectivity between 40 and 50 dBZ. As reflectivity increases, the CSU-HIDRO algorithm increasingly relies on ZDR and KDP to retrieve rain rate, whereas

TRMM PR relies solely on Z-R relationships. KDP is especially useful when reflectivity has significant contributions from hail, responding primarily to the number concentration of oblate hydrometeors, while ZDR limits retrieved rain rates from horizontal reflectivity when oblate raindrops are present. The higher WSR-88D rain rates for a given reflectivity combine with the higher low level reflectivities for a given maximum 40 dBZ height to produce much greater mean rainfall rates than TRMM PR as a function of maximum 40 dBZ echo height. Mean WSR-88D retrieved rainfall rates are consistently 15 – 20 mm hr^{-1} greater than TRMM-Ku and TRMM-S retrieved mean rainfall rates for a given maximum 40 dBZ height when maximum 40 dBZ echo heights extend above 5 km.

Mean vertical profiles of reflectivity as a function of maximum 40 dBZ height show that TRMM PR and WSR-88D agree to within 1 dBZ when maximum 40 dBZ heights are below 5 km. However, as soon as the maximum 40 dBZ height penetrates above 5 km, TRMM PR reflectivity below the melting level becomes offset lower than WSR-88D. For extreme maximum 40 dBZ heights between 10 and 15 km, WSR-88D produces a mean reflectivity profile that is greater than TRMM-Ku and TRMM-S profiles at nearly all vertical levels. These results indicate that the 2A25 V7 algorithm becomes increasingly biased toward lower reflectivity and rain rate as graupel and hail content increases in the column.

Revisiting the idea of the overlap fraction between extreme convective intensity and extreme rain rate, WSR-88D has an overlap fraction of 99th percentile maximum 40 dBZ height and 99th percentile low-level rain rate that is 31% greater than retrieved by TRMM-S. The overlap fraction of 99th percentile maximum 40 dBZ height and 99th percentile low-level reflectivity is an astounding 259% greater for WSR-88D than TRMM-

S. While the overlap percentage indicated by WSR-88D between these extreme variables is still low (~10% for maximum 40 dBZ height and 1.5 km rain rate; ~20% for maximum 40 dBZ height and 1.5 km reflectivity), overlap percentages retrieved by TRMM PR appear to be negatively biased.

Examinations of PIA, KDP, ZDR, and hail fraction provide insight to potential causes of differences between WSR-88D and TRMM PR retrievals. Mean TRMM PR PIA increases with increasing maximum 40 dBZ heights, however the greatest median PIA values are associated with the highest rain rates, which exist in columns that have more limited maximum 40 dBZ echo heights reaching between 5 and 9 km. 1.5-km altitude hail fraction, retrieved using a WSR-88D PID algorithm, increases with increasing maximum 40 dBZ height and 1.5-km reflectivity, indicating that the TRMM PR attenuation correction algorithm is possibly misidentifying low-mid level ice as greater attenuating liquid in these cases. Mean WSR-88D KDP and ZDR are dual-polarization variables that respond to oblate hydrometeors that were not retrievable by TRMM PR, but are useful in retrieving more accurate rain rates. Both increase with increasing rain rates and reflectivities, meaning drop size distributions are changing with reflectivity and rain rate in a manner that is not observable by TRMM. Mean ZDR levels off once rain rates reach 40 mm hr^{-1}, but the highest values of KDP are associated with the highest rain rates and reflectivities, which are also areas of significant mean PIA for TRMM PR.

Overall, comparisons between WSR-88D and TRMM PR indicate that errors in the estimated PIA and/or attenuation correction method (assumed phase, particle size distribution, and/or attenuation coefficients) in the 2A25 V7 algorithm are contributing to low level reflectivities that are biased low. Usage of KDP to retrieve high rain rates also

indicates that 2A25 V7 Z-R relationships may be underestimating rain rates for intense convection, except in rare situations of extreme low level reflectivity exceeding 55 dBZ, where the Z-R relationship overestimates rain rate because of likely hail contamination.

5.2 Uncertainties and Future Work

For this study, WSR-88D rain rates were calculated at a horizontal resolution of 1.125-km using the CSU-HIDRO (Cifelli et al. 2011) algorithm. To further analyze the comparison between WSR-88D retrieved rain rates and TRMM PR retrieved rain rates, this study could be expanded to include other WSR-88D rain rate calculations that use different coefficients for different Z-R, Z-ZDR-R, KDP-ZDR-R, and KDP-R relationships, such as those found in Sachidananda and Zrnic (1987), Ryzhkov and Zrnic (1995), and Brandes et al. (2002).

Additionally, in order to more directly compare WSR-88D S-band reflectivities to TRMM PR Ku-band reflectivities, Ku-band reflectivities were converted to equivalent S-band retrievals (Cao et al. 2013). For this study, the coefficients for rain were used below altitudes of 3.5 km and coefficients for dry hail, as defined in Cao et al. (2013), were used above 5 km. The impact of the assumed hydrometeor type by height, and the coefficients used, could be tested to address potential bias in the analysis resulting from the conversion of Ku-band to S-band.

Thirdly, the WSR-88D data in this study is only analyzed from volume coverage patterns (VCPs) 11, 12, 211, and 212, which are convective scan strategies. While these VCPs scan at 14 different elevation angles, VCP 12 has a higher concentration of low-level scans. Future work could include comparison between the different scan types and results

as a function of range from the radar to assess potential biases in the vertical reflectivity profile that results from specific scan strategies.

The low bias present in retrieved low level TRMM PR reflectivities relative to WSR-88D reflectivities when maximum 40 dBZ heights extend above the melting level is also worth further investigation. At low levels, TRMM-Ku is expected to retrieve higher reflectivities than WSR-88D after attenuation correction, however these findings show that it retrieves consistently lower reflectivities than WSR-88D as maximum 40 dBZ echo heights increase above the melting level. To investigate this bias, a similar comparison of vertical reflectivity profiles should be conducted over the ocean using WSR-88Ds located along the Gulf of Mexico coastline. Over water, the surface reflectivity is more certain than over land, meaning PIA estimates in the TRMM PR 2A25 algorithm can be better trusted. With limited PIA contributions to reflectivity biases over the ocean, the separate contributions of PIA and inaccurate assumptions of phase and hydrometeor size distribution vertical profiles to biases can be analyzed through comparison of land and ocean statistics that control for factors such as maximum 40 dBZ height.

Lastly, with the launch of the Global Precipitation Measurement (GPM) satellite in 2014, there is an opportunity to add GPM observations over the same domain to the analysis as well as to expand the comparison to higher latitudes, as GPM orbits between 65 °N and 65 °S. The addition of GPM data would aid an assessment of potential biases present in the retrievals of the Dual-frequency Precipitation Radar (DPR) to analyze whether rain rate and reflectivity estimates for intense convection have improved over those from the TRMM PR.

REFERENCES

Adler, R. F., Wang, J., Gu, G., & Huffman, G. J. (2009). A Ten-Year Tropical Rainfall Climatology Based on a Composite of TRMM Products. *Journal of the Meteorological Society of Japan. Ser. II*, *87*, 281–293. https://doi.org/http://doi.org/10.2151/jmsj.87A.281

Amitai, E., Wolff, D. B., Marks, D. A., & Silberstein D. S. (2002). Radar rainfall estimation: lessons learned from the NASA/TRMM validation program. *ERAD 2002*, 255–260.

Berkowitz, D. S., Schultz, J. A., Vasiloff, S., Elmore, K. L., Payne, C. D., & Boettcher, J. B. (2013). Status of dual pol QPE in the WSR-88D network. *93th AMS, 27th Conference on Hydrology*, *i*(Ic).

Brandes, E. A., Ryzhkov, A. V., & Zrnić, D. S. (2001). An evaluation of radar rainfall estimates from specific differential phase. *Journal of Atmospheric and Oceanic Technology*, *18*(3), 363–375. https://doi.org/10.1175/1520-0426(2001)018<0363:AEORRE>2.0.CO;2

Brandes, E. A., Zhang, G., & Vivekanandan, J. (2002). Experiments in Rainfall Estimation with a Polarimetric Radar in a Subtropical Environment. *Journal of Applied Meteorology*, *41*(6), 674–685. https://doi.org/10.1175/1520-0450(2002)041<0674:EIREWA>2.0.CO;2

Cao, Q., Hong, Y., Qi, Y., Wen, Y., Zhang, J., Gourley, J. J., & Liao, L. (2013). Empirical conversion of the vertical profile of reflectivity from Ku-band to S-band frequency. *Journal of Geophysical Research Atmospheres*, *118*(4), 1814–1825. https://doi.org/10.1002/jgrd.50138

Chandrasekar, V., Hou, A., Smith, E., Bringi, V. N., Rutledge, S. A., Gorgucci, E., … Jackson, G. S. (2008). Potential role of dual-polarization radar in the validation of satellite precipitation measurements: Rationale and opportunities. *Bulletin of the American Meteorological Society*, *89*(8), 1127–1145. https://doi.org/10.1175/2008BAMS2177.1

Cifelli, R., Chandrasekar, V., Lim, S., Kennedy, P. C., Wang, Y., & Rutledge, S. A. (2011). A new dual-polarization radar rainfall algorithm: Application in Colorado precipitation events. *Journal of Atmospheric and Oceanic Technology*, *28*(3), 352–364. https://doi.org/10.1175/2010JTECHA1488.1

Crum, T. D., & Alberty, R. L. (1993). The WSR-88D and the WSR-88D Operational Support Facility. *Bulletin of the American Meteorological Society*. https://doi.org/10.1175/1520-0477(1993)074<1669:TWATWO>2.0.CO;2

Cunha, L. K., Smith, J. A., Krajewski, W. F., Baeck, M. L., & Seo, B.-C. (2015). NEXRAD NWS Polarimetric Precipitation Product Evaluation for IFloodS. *Journal of Hydrometeorology*, *16*(4), 1676–1699. https://doi.org/10.1175/JHM-D-14-0148.1

Gorgucci, E., Scarchilli, G., & Chandrasekar, V. (1994). A Robust Estimator of Rainfall Rate Using Differential Reflectivity. *Journal of Atmospheric and Oceanic Technology*. https://doi.org/10.1175/1520-0426(1994)011<0586:AREORR>2.0.CO;2

Hamada, A., Takayabu, Y. N., Liu, C., & Zipser, E. J. (2015). Weak linkage between the heaviest rainfall and tallest storms. *Nature Communications*, *6*, 6213. https://doi.org/10.1038/ncomms7213

Hence, D. A., & Houze, R. A. (2011). Vertical Structure of Hurricane Eyewalls as Seen by the TRMM Precipitation Radar. *Journal of the Atmospheric Sciences*, *68*(8), 1637–1652. https://doi.org/10.1175/2011JAS3578.1

Hitschfeld, W., Bordan, J., Hitschfeld, W., & Bordan, J. (1954). Errors Inherent in the Radar Measurement of Rainfall At Attenuating Wavelengths. *Journal of Meteorology*. https://doi.org/10.1175/1520-0469(1954)011<0058:EIITRM>2.0.CO;2

Iguchi, T., Meneghini, R., Awaka, J., Kozu, T., & Okamoto, K. (2000). Rain profiling algorithm for TRMM Precipitation Radar data. *Advances in Space Research*, *25*(5), 973–976. https://doi.org/10.1016/S0273-1177(99)00933-3

Iguchi, T., Kozu, T., Kwiatkowski, J., Meneghini, R., Awaka, J., & Okamoto, K. 'ichi. (2009). Uncertainties in the Rain Profiling Algorithm for the TRMM Precipitation Radar. *Journal of the Meteorological Society of Japan*, *87*, 1–30. https://doi.org/10.2151/jmsj.87A.1

Iguchi, T., & Meneghini, R. (1994). Intercomparison of Single-Frequency Methods for Retrieving a Vertical Rain Profile from Airborne or Spaceborne Radar Data. *Journal of Atmospheric and Oceanic Technology*. https://doi.org/10.1175/1520-0426(1994)011<1507:IOSFMF>2.0.CO;2

Istok, M. J., Fresch, M., Jing, Z., Smith, S. D., Murnan, R., Ryzhkov, A., … Saffle, R. E. (2009). Wsr-88D Dual Polarization Initial Operational Capabilities. *25th Conference on International Interactive Information and Processing Systems (IIPS) for Meteorology, Oceanography, and Hydrology*, (January).

Jiang, H., & Zipser, E. J. (2010). Contribution of Tropical Cyclones to the Global

Precipitation from Eight Seasons of TRMM Data: Regional, Seasonal, and Interannual Variations. *Journal of Climate*, *23*(2005), 1526–1543. https://doi.org/10.1175/2009JCLI3303.1

Kirstetter, P. E., Hong, Y., Gourley, J. J., Schwaller, M., Petersen, W., & Zhang, J. (2012). Comparison of TRMM 2A25 Products Version 6 and Version 7 with NOAA/NSSL Ground Radar-based National Mosaic QPE. *Journal of Hydrometeorology*, 121018124559005. https://doi.org/10.1175/JHM-D-12-030.1

Kozu, T., Iguchi, T., Shimomai, T., & Kashiwagi, N. (2009). Raindrop size distribution modeling from a statistical rain parameter relation and its application to the TRMM precipitation radar rain retrieval algorithm. *Journal of Applied Meteorology and Climatology*, *48*(4), 716–724. https://doi.org/10.1175/2008JAMC1998.1

Kummerow, C., Barnes, W., Kozu, T., Shiue, J., & Simpson, J. (1998). The tropical rainfall measuring mission(TRMM) sensor package. *Journal of Atmospheric and Oceanic Technology*, *15*(3), 809–817. https://doi.org/10.1175/1520-0426(1998)015<0809:TTRMMT>2.0.CO;2

Kummerow, C., Simpson, J., Thiele, O., Barnes, W., Chang, a. T. C., Stocker, E., … Nakamura, K. (2000). The Status of the Tropical Rainfall Measuring Mission (TRMM) after Two Years in Orbit. *Journal of Applied Meteorology*, *39*(12), 1965–1982. https://doi.org/10.1175/1520-0450(2001)040<1965:TSOTTR>2.0.CO;2

Kummerow, C., Hong, Y., Olson, W. S., Yang, S., Adler, R. F., McCollum, J., … Wilheit, T. T. (2001). The Evolution of the Goddard Profiling Algorithm (GPROF) for Rainfall Estimation from Passive Microwave Sensors. *Journal of Applied Meteorology*, *40*(11), 1801–1820. https://doi.org/10.1175/1520-0450(2001)040<1801:TEOTGP>2.0.CO;2

Liao, L., & Meneghini, R. (2009). Validation of TRMM precipitation radar through comparison of its multiyear measurements with ground-based radar. *Journal of Applied Meteorology and Climatology*, *48*(4), 804–817. https://doi.org/10.1175/2008JAMC1974.1

Liao, L., Meneghini, R., & Iguchi, T. (2001). Comparisons of rain rate and reflectivity factor derived from the TRMM precipitation radar and the WSR-88D over the Melbourne, Florida, site. *Journal of Atmospheric and Oceanic Technology*, *18*(12), 1959–1974. https://doi.org/10.1175/1520-0426(2001)018<1959:CORRAR>2.0.CO;2

Liu, C., & Zipser, E. J. (2005). Global distribution of convection penetrating the tropical tropopause. *Journal of Geophysical Research Atmospheres*, *110*(23), 1–12. https://doi.org/10.1029/2005JD006063

Liu, C., Zipser, E. J., Cecil, D. J., Nesbitt, S. W., & Sherwood, S. (2008). A cloud and precipitation feature database from nine years of TRMM observations. *Journal of Applied Meteorology and Climatology*, *47*(10), 2712–2728. https://doi.org/10.1175/2008JAMC1890.1

Liu, C., Zipser, E. J., & Nesbitt, S. W. (2007). Global distribution of tropical deep convection: Different perspectives from TRMM infrared and radar data. *Journal of Climate*, *20*(3), 489–503. https://doi.org/10.1175/JCLI4023.1

Lonfat, M., Marks, F. D., & Chen, S. S. (2004). Precipitation Distribution in Tropical Cyclones Using the Tropical Rainfall Measuring Mission (TRMM) Microwave Imager: A Global Perspective. *Monthly Weather Review*, *132*(7), 1645–1660. https://doi.org/10.1175/1520-0493(2004)132<1645:PDITCU>2.0.CO;2

Marks, D. A., Kulie, M. S., Robinson, M., Silberstein, D. S., Wolff, D. B., Ferrier, B. S., Amitai, E., Fisher, B., Wang, J., Augustine, D., & Thiele, O. (2000). Climatological processing and product development for the TRMM ground validation program. *Physics and Chemistry of the Earth, Part B: Hydrology, Oceans and Atmosphere*, *25*(10-12), 871–875. https://doi.org/10.1016/S1464-1909(00)00118-0

Meneghini, R., Iguchi, T., Kozu, T., Liao, L., Okamoto, K., Jones, J. A., & Kwiatkowski, J. (2000). Use of the Surface Reference Technique for Path Attenuation Estimates from the TRMM Precipitation Radar. *Journal of Applied Meteorology*, *39*(12), 2053–2070. https://doi.org/10.1175/1520-0450(2001)040<2053:UOTSRT>2.0.CO;2

Nesbitt, S. W., Cifelli, R., & Rutledge, S. a. (2006). Storm Morphology and Rainfall Characteristics of TRMM Precipitation Features. *Monthly Weather Review*, *134*(10), 2702–2721. https://doi.org/10.1175/MWR3200.1

Nesbitt, S. W., & Zipser, E. J. (2003). The diurnal cycle of rainfall and convective intensity according to three years of TRMM measurements. *Journal of Climate*, *16*(10), 1456–1475. https://doi.org/10.1175/1520-0442-16.10.1456

Petersen, W. A., & Rutledge, S. A. (2001). Regional variability in tropical convection: Observations from TRMM. *Journal of Climate*, *14*(17), 3566–3586. https://doi.org/10.1175/1520-0442(2001)014<3566:RVITCO>2.0.CO;2

Rasmussen, K. L., Choi, S. L., Zuluaga, M. D., & Houze, R. A. (2013). TRMM precipitation bias in extreme storms in South America. *Geophysical Research Letters*, *40*(13), 3457–3461. https://doi.org/10.1002/grl.50651

Ryzhkov, A. V., & Zrnić, D. S. (1995). Comparison of Dual-Polarization Radar Estimators of Rain. *Journal of Atmospheric and Oceanic Technology*. https://doi.org/10.1175/1520-0426(1995)012<0249:CODPRE>2.0.CO;2

Ryzhkov, A. V., & Zrnic, D. S. (1996). Assessment of rainfall using Specific Differential Phase (KDP). *Journal of Applied Meteorology*. https://doi.org/10.1175/1520-0450(1996)035<2080:AORMTU>2.0.CO;2

Sachidananda, M., & Zrnić, D. S. (1987). Rain rate estimates from differential polarization measurements. *Journal of Atmospheric and Oceanic Technology*. https://doi.org/http://dx.doi.org/10.1175/1520-0426(1987)004<0588:RREFDP>2.0.CO;2

Schumacher, C., & Houze, R. A. (2003). Stratiform rain in the tropics as seen by the TRMM precipitation radar. *Journal of Climate*, *16*(11), 1739–1756. https://doi.org/10.1175/1520-0442(2003)016<1739:SRITTA>2.0.CO;2

Simpson, J., Adler, R. F., & North, G. R. (1988). A Proposed Tropical Rainfall Measuring Mission (TRMM) Satellite. *Bulletin of the American Meteorological Society*. https://doi.org/10.1175/1520-0477(1988)069<0278:APTRMM>2.0.CO;2

Wang, J. J., Adler, R. F., Huffman, G. J., & Bolvin, D. (2014). An updated TRMM composite climatology of tropical rainfall and its validation. *Journal of Climate*, *27*(1), 273–284. https://doi.org/10.1175/JCLI-D-13-00331.1

Wolff, D. B., Marks, D. A., Amitai, E., Silberstein, D. S., Fisher, B. L., Tokay, A., Wang, J., & Pippitt, J. L. (2005). Ground validation for the tropical rainfall measuring mission (TRMM). *Journal of Atmospheric and Oceanic Technology*, *22*(4), 365–380. https://doi.org/10.1175/JTECH1700.1

Zipser, E. J., Cecil, D. J., Liu, C., Nesbitt, S. W., & Yorty, D. P. (2006). Where are the most: Intense thunderstorms on Earth? *Bulletin of the American Meteorological Society*, *87*(8), 1057–1071. https://doi.org/10.1175/BAMS-87-8-1057

Zipser, E. J., & Lutz, K. R. (1994). The vertical profile of radar reflectivity of convective cells: A strong indicator of storm intensity and lightning probability? *Monthly Weather Review*. https://doi.org/10.1175/1520-0493(1994)122<1751:TVPORR>2.0.CO;2